Advancing Structural Batteries using Lithium-Iron Phosphate Functionalised High-Modulus Carbon Fibres Positive Electrodes

Master Thesis in Industrial and Materials Science

Anastasiia Marchenko and Hlib Kavatsiuk

DEPARTMENT OF INDUSTRIAL AND MATERIALS SCIENCE

CHALMERS UNIVERSITY OF TECHNOLOGY

Gothenburg, Sweden 2024

www.chalmers.se

Degree project report 2024

Advancing Structural Batteries using Lithium-Iron Phosphate Functionalised High-Modulus Carbon Fibres Positive Electrodes

Anastasiia Marchenko and Hlib Kavatsiuk

CHALMERS
UNIVERSITY OF TECHNOLOGY

Department of Industrial and Materials Science
Chalmers University of Technology
Gothenburg, Sweden 2024

Advancing Structural Batteries using Lithium-Iron Phosphate Functionalised High-Modulus Carbon Fibres Positive Electrodes
Anastasiia Marchenko and Hlib Kavatsiuk

Supervisor: dr. Richa Chaudhary, Department of Industrial and Materials Science
Supervisor: dr. Johanna Xu, Department of Industrial and Materials Science
Examiner: prof. Leif Asp, Department of Industrial and Materials Science

Degree project report 2024
Department of Industrial and Materials Science
Chalmers University of Technology
SE-412 96 Gothenburg
Sweden
Telephone +46 31 772 1000

Cover: image is AI-generated using ChatGPT 4 and illustrates the concept of using structural batteries in aircraft.

Typeset in LaTeX
Gothenburg, Sweden 2024

Advancing Structural Batteries using Lithium-Iron Phosphate Functionalised High-Modulus Carbon Fibres Positive Electrodes

Anastasiia Marchenko and Hlib Kavatsiuk
Department of Industrial and Materials Science
Chalmers University of Technology

Abstract

This thesis explores the advancement of structural batteries by utilising nanosized lithium-iron phosphate functionalised high-modulus carbon fibres as positive electrodes. The innovative laminated structural battery architecture integrates active electrode materials with structural battery electrolyte, facilitating both mechanical load-bearing and ionic transport. We employed the electrophoretic deposition technique to coat CFs with a blend of nano-LFP, carbon black, and reduced graphene oxide in an ethanol suspension, enhanced by PDDA as a cationic polyelectrolyte.

The study's experimental phase optimised EPD parameters (70-80 V for 5-20 minutes), achieving uniform coatings with active material mass ranging between 12-35 mg. Electrochemical performance was evaluated through cyclic voltammetry, galvanostatic charge-discharge, and electrochemical impedance spectroscopy. Half-cell results demonstrated that positive electrodes with nanosized LFP and high-modulus CFs exhibit promising potential for structural batteries, showing specific capacities and stable cycling behaviour. However, all-fibre full cells indicated the necessity for further research.

The integration of CB and rGO significantly improved the electronic conductivity and structural stability of the electrodes, contributing to enhanced overall battery efficiency. This work highlights the potential of functionalised high-modulus CFs in advancing the field of structural batteries, addressing both energy storage and mechanical integrity, crucial for future applications in electric vehicles and other weight-sensitive technologies.

Keywords: structural batteries, carbon fibre composites, multifunctional materials, lithium-ion batteries, electrophoretic deposition.

Acknowledgements

We extend our deepest gratitude to several individuals who have played instrumental roles throughout the duration of this thesis.

Our examiner, Professor Leif Asp, whose enthusiasm and passion were incredibly motivating at every encounter. Despite his busy schedule, his guidance was always illuminating, making each meeting feel like a ray of sunshine in often grey Göteborg. His support has been invaluable, and for that, we are immensely grateful.

We owe a tremendous debt of gratitude to our supervisor, Dr. Richa Chaudhary, who has been with us from the very beginning. Her unwavering support and dedication have been the backbone of our journey. Her responsibility and commitment to our project have been second to none, and we cannot thank her enough for her guidance and valuable tips for our future research career.

Our co-supervisor, Dr. Johanna Xu, who has been a pivotal help throughout our projects during the track course and master's research. We deeply appreciate the time and effort she invested in us and her invaluable assistance around the lab.

We are also thankful to the entire division of Material and Computational Mechanics for providing us the opportunity to conduct our research and write our thesis within such a stimulating environment. Special thanks go to Carl Larsson, Ruben Tavano, Huixin Chen, and Emelie Seignér for their cheerful smiles in the corridors and the enriching discussions we shared during meetings and lunch breaks.

Hlib Kavatsiuk would like to extend a special thank you to the members of the HTC centre, particularly Matthieu Thomas, Mareddy Reddy, Jan Froitzheim, Anton Chyrkin, and Thorbjørn Krogsgaard. Their continuous support and guidance throughout my time at HTC and during the thesis process have been fundamental to my academic and professional growth. Their advice and practical tips have undoubtedly eased the challenges of thesis writing.

We must also express our profound appreciation to our parents and families, whose unwavering support and sacrifices have made our studies at Chalmers possible. Without their encouragement and support, we would not have had the opportunity to study in Sweden and embark on this incredible academic journey.

Together, Anastasiia and Hlib, we are grateful to everyone who contributed to our journey. Your support and encouragement have been pillars of our success.

Anastasiia Marchenko and Hlib Kavatsiuk, Gothenburg, June 2024

List of Acronyms

Below is the list of acronyms that have been used throughout this thesis listed in alphabetical order:

AIBN	Azobisisobutyronitrile
APS	Average Particle Size
BES	Battery Energy Storage
CB	Carbon Black
CF	Carbon Fibres
CV	Cyclic Voltammetry
DCM	Dichloromethane
EC	Ethylene carbonate
EIS	Electrochemical Impedance Spectroscopy
EPD	Electrophoretic Deposition
EV	Electric Vehicle
FC	Full Cell
GCD	Galvanostatic Charge-Discharge
HC	Half-Cell
HM	High Modulus
IM	Intermidiate Modulus
LFP	Lithium Iron Phosphate
LIB	Lithium-ion Battery
LiTFSI	Lithium bis(trifluoromethanesulfonyl)imide
OCP	Open Circuit potential
PAN	Polyacrylonitrile
PC	Propylene carbonate
PDDA	Poly(diallyldimethylammonium chloride)
PE	Polyethylene
PET	Polyethylene terephthalate
PU	Polyurethane
rGO	Reduced Graphene Oxide
SB	Structural Battery
SBC	Structural Battery Composite
SBE	Structural Battery Electrolyte
SEM	Scanning Electron Microscopy
UHM	Ultra-High Modulus

Contents

List of Figures

List of Tables

1

Introduction

"Innovation is seeing what everybody has seen and thinking what nobody has thought."
— Dr. Albert Szent-Györgyi

From the mid-to-late 18th century, humanity embarked on a challenge to harness the unique phenomenon of electricity for practical storage. Throughout history, the realisation of energy storage devices progressed steadily toward the electric battery technology as we know it today[1].

The journey starts from the prototype of capacitors - Leyden's jar (1745), which inspired Benjamin Franklin to coin the term *battery* and describe the concept behind electricity storage device (1749), yet the "Machine" rather resembled the early capacitor[2]. Since then, multiple electrochemical cell device originating from the French word, *batterie*, is meant to represent "a group of two or more similar objects functioning together" up to years ahead. Three years later the same Leyden jars played a pivot role in one of the most striking scientific experiments - harnessing lightning electricity with kite[3]. Then the *battery* story continued unwinding through the unmasking of the "animal electricity" misconception, also widely associated with so-called *frog experiments* conducted by Luigi Galvani (1780). At that time this discovery divided the scientific community into two opposing groups - the ones that believed in animal electricity as the new form of energy, and the ones that were skeptical about the idea. The discovery intrigued society and became an aspiration for Alessandro Volta to invent the first true electric battery, which was a fruitful result of mimicking the *frog experiment*[4]. Volta proved that the electric potential of different metals is the cause of the current flow in the frog's limb by publishing his invention of Voltaic Pile, the first electric battery[5]. Further, in time, the battery story witnessed both fast-moving and stagnation periods, the arrival of the first mass production batteries sealed in wooden boxes (1802)[6] and rechargeable batteries (1859)[7], culminating in the development of alkaline (1899)[8] and commercially available lithium-based batteries (1970s)[9]. However, the currently recognised invention of the electric battery attributed to Alessandro Volta took place in 1800[5], meaning that it has been for over 200 years, and still, today battery technology manages to keep the intrigue of making astounding contributions to modern society.

Subsequently, the development of electrochemical energy storage continues to advance dispersively across numerous research areas. In general, the development trajectory aligns well with the Olympic motto: striving for "Faster, Higher, Stronger" battery technology. Nevertheless, various challenges come into play that cannot be ignored to approach modern concerns: environmental sustainability, safety, and cost

reduction[10].

Globally, the biggest fractions of economic sectors contributing the most to total greenhouse gas emissions are electricity generation for industrial and living purposes, and transportation[11]. Decarbonisation via electrification means stands out as the foremost solution to the climate impact challenges faced by the transportation sector. However, the costs and electric vehicle efficiency are still significant obstacles standing in the way. To address these two stumbling blocks simultaneously, a game-changer — the multifunctional material concept — can be utilised. This concept involves integrating multiple functions within one material, significantly reducing its mass and achieving higher efficiency[12].

State-of-the-art battery composite manifests such material carrying both mechanical load and electrical storage while reducing the total mass of the device. The first realisation of structural power material was achieved by Wetzel and his team at the Army Research Laboratories in the USA in 2007. Although the device showed unbalanced effectiveness between mechanical and electrochemical properties[13].

Nowadays, multifunctional composite materials have attracted considerable attention across various research fields. Specifically, "mass-less" energy storage is on the radar as a lightweight alternative to standard Li-ion batteries. The increased interest is additionally fuelled in the light of forthcoming stricter EU regulations on greenhouse gas emissions[14]. This fascination is not unexpected, given that structural power technologies offer not only one of the strategies to meet these requirements but also a promising step towards improving resource efficiency. The combination of all these advantages makes research in the area of structural power particularly valuable for the automotive, aeronautic, and marine sectors in our low-carbon future[14].

1.1 Background

1.1.1 Battery concept

A battery is a device that converts chemical energy stored in the electrodes' active material directly into electric energy through an electrochemical redox reaction. The fundamental unit in which redox reaction occurs is an electrochemical cell, whereas batteries consist of one or more such cells. Each full electrochemical cell comprises three main components: the anode (negative electrode), which releases electrons and oxidises during the reaction during discharging; the cathode (positive electrode; source of positive ions), which accepts electrons from the external circuit being reduced when discharged; and the electrolyte - a medium enabling ion transfer, but not the electron one, between the anode and cathode[6,15,16].

Using conventional lithium-ion batteries as an example, the positive electrode material is typically a metal oxide, such as $LiCoO_2$, $LiMn_2O_4$, or $LiFePO_4$ connected to an aluminum foil current collector, and the negative electrode material is graphite carbon on a copper current collector. During charge/discharge processes, lithium ions are intercalated and extracted between atomic layers of active materials[6]. LIB, as a representative of widely commercialised battery technology, has a high specific energy and energy density, rendering it valuable for weight- and volume-sensitive

applications[6]. However, they have almost reached a plateau in their ability to provide increased capacity, power, and lifetime for a given weight and cost, as indicated by demand assessments and research[11,17,18], and structural power composite is one of the technologies with the real potential to address this challenge for LIBs.

1.1.2 Multifunctional structural power composite concept

There are essentially two strategies for realising the concept of multifunctionality. One of them represents a multifunctional structure, where the material adding the desired functionality is implanted within a parent one. The other strategy perceives multifunctionality as a unit comprising structural constituents that provide simultaneously and synergistically two or more functions[19]. In that way, a truly multifunctional material, for example, polymer composites, can undergo mechanical loads, store and deliver electrical energy, while also enabling mass reduction and preserving or even enhancing the intrinsic properties of individual components[19].

Considering an EV battery pack, the lithium-ion battery pack in a Tesla Model S contributes approximately 30% to the vehicle's total mass. Simplifying the vehicle into two main components — energy storage and exterior structure — reveals that the exterior structure does not contribute to energy storage, and the energy storage system does not provide structural benefits. This separation increases the total vehicle weight, reducing efficiency. However, using multifunctional structural composite materials can address both needs, providing structural integrity and energy storage while reducing the overall mass, as depicted in Figure 1.1[20].

Figure 1.1. Structural power concept expressed in simple math relation.

1.1.3 Laminated structural battery concept

Laminated structural battery composite represents the current state-of-the-art architecture of structural batteries, consisting of two CF-reinforced electrodes, a separator, and a bi-continuous electrolyte material known as structural battery electrolyte. As a truly multifunctional composite, each constituent contributes to multifunctionality, a goal that has encountered persistent challenges from the development side of the positive electrode. In previous studies, LFP foil was commonly used as a positive electrode in laminated SBCs, deviating from the concept of a truly multifunctional material[14,21,22]. Successful results have been achieved in the realisation of true SB multifunctionality in the paper of Sanchez et al.[23], where full battery cells

were produced using chemically functionalised CF as the cathodic material, instead of LFP foil. These results indicate the importance of further research on positive electrode coating as one of the top priorities for SB advancements.

1.2 Aim and Limitations/Demarcations

The primary aim of this thesis is to explore the use of novel active materials, particularly focusing on positive electrode development, to enhance the mechanical load-bearing capabilities and conductivity efficiency of laminated structural batteries. By advancing these multifunctional capabilities, this work aims to address the evolving challenges faced in modern energy storage systems, particularly in the context of electric vehicles and other applications where weight and efficiency are critical.

However, the scope of this study is delineated by certain limitations. The research does not focus on identifying the most optimal coating features required for the most efficient cathode material. Additionally, aspects such as life cycle assessment and the production of comprehensive safety data are excluded from this thesis. The primary emphasis remains on the material and electrochemical performance enhancements rather than on a holistic evaluation of all potential factors influencing structural battery performance.

2

Theory

"The aim of science is to seek the simplest explanations of complex facts. We are apt to fall into the error of thinking that the facts are simple because simplicity is the goal of our quest."

— *Alfred North Whitehead*

In the quest for simplicity amidst complexity, science often unveils elegantly simple explanations for the intricate phenomena that define our world. This pursuit is vividly reflected in the development of structural batteries, a frontier marrying material science and energy storage to reshape the landscape of electric mobility. The following sections delve into the theoretical foundations and practical implementations of this innovation. We explore the laminated structural battery architecture, carbon fibre-based electrodes, the electrochemistry governing lithium-ion battery cells, and the process of electrophoretic deposition. Each topic builds on the last, unfolding a narrative of how simple solutions can address complex challenges in energy storage and structural functionality.

2.1 Laminated SB architecture

The laminated structural battery architecture, depicted in Figure 2.1, embodies a sophisticated approach to energy storage and structural integrity. In this configuration, the various components of a typical battery cell are transformed into layers within a laminate structure. This includes the active materials for the negative and positive electrodes, which are interspersed by a separator. These components are encapsulated within a bi-continuous polymer known as the structural battery electrolyte. The SBE incorporates a liquid electrolyte that not only facilitates ionic transport essential for battery function but also contributes to the mechanical load-bearing capabilities of the structure. This dual functionality is pivotal for applications where structural integrity and energy storage are equally critical[24].

2.2 CF-based electrodes

Carbon fibre (CF) is a lightweight, strong material composed of thin, crystalline filaments of graphitised carbon atoms[25]. Known for its high mechanical strength

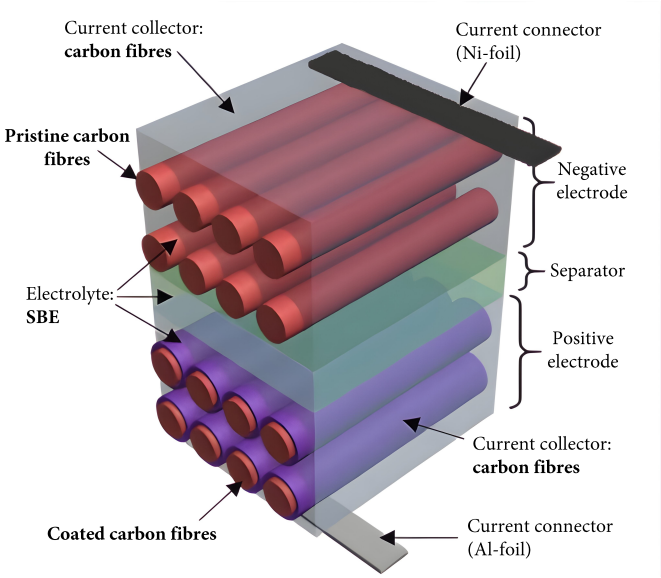

Figure 2.1. Schematic illustration of the laminated SB architecture, adapted from Carlstedt et. al[24].

and stiffness, CF is also an excellent conductor of electricity and, therefore is a strong candidate for electrode material in SBs[20].

CF provides with the ability for diffusive intercalation of lithium ions into the carbon layers at a low electrode potential (-3.045 V measured against the standard hydrogen electrode). CFs are characterised by various grades defined by the modulus of elasticity, which is a measure of stress necessary to cause a material's deformation. There are standard modulus [230-250] GPa, intermediate modulus [300-315] GPa, high modulus [350-400] GPa, and ultra-high modulus often exceeding 450 GPa CFs types. Generally, the higher stiffness CFs exhibit the lower tensile strength, which is the measure of material's failure once exposed to the stress[26–28]. PAN-based CFs have a tensile strength ranging from 2 up to 7 GPa, corresponding to an intermediate modulus of 300 GPa, which makes the material low failure strained (about 2%) and characterised by linear elastic behaviour until failure[20,28]. Intermediate modulus CF possesses a turbostratic graphitic structure allowing lithium ions for reversible intercalation while acting as a host during charging and discharging cycles. Turbostratic structure means that carbon layers formed into fibrils of crystallites are arranged in random directions, shifted and folded, but aligned parallel to each other, meaning that fibre structure includes sp^3 hybridised carbons as well[20,29]. CF microstructure contains crystal and amorphous regions, the fraction of which decides the properties. The average crystallite size values increase for higher modulus fibres, whereas the average crystallite interlayer spacing is decreased with increasing degrees of graphitisation, which means that higher heat treatment temperature was used[29]. For intermediate and high modulus CF typical values of crystallite size are 2 and 11 nm in length, respectively.[30] The pure graphite interlayer spacing is 3.35 Å, while PAN-based CFs generally have higher values and can vary from 3.60 Å for low modulus fibres down to 3.40 Å for high modulus fibres[31].

As for the electrical properties of CFs, the conductivity is reported to increase

as a function of the growing degree of graphitisation, as then fibres resemble the ideal graphite structure (higher degree of crystallinity and preferred orientation)[32]. Moreover, electrochemical characterisation studies have shown that intermediate modulus polyacrylonitrile (PAN) -based CF exhibits the highest electrochemical capacities in comparison to the other fibre grades[20]. Therefore, CF's mechanical and electrochemical properties make it a highly suitable material for electrode reinforcement in SBCs[20,25].

2.3 Electrochemistry inside LIB cell

Redox reactions in batteries are the essence of storage and conversion of chemical energy into electrical energy. The electrochemical reactions occurring on the cathode and anode respectively are as follows:

$$\mathrm{LiMO_2} \rightleftarrows \mathrm{Li_{1-x}MO_2} + \mathrm{xLi^+} + \mathrm{xe^-}, \tag{2.1}$$

$$\mathrm{C} + \mathrm{xLi^+} + \mathrm{xe^-} \rightleftarrows \mathrm{Li_xC}. \tag{2.2}$$

Combining the equations above the full redox reaction is obtained:

$$\mathrm{LiMO_2} + \mathrm{C} \rightleftarrows \mathrm{Li_xC} + \mathrm{Li_{1-x}MO_2}, \tag{2.3}$$

where MO_2 represents a metal oxide, C is a graphite plane in negative electrode material. During lithiation, Li ions situated on the cathode material (2.1) move to the anode to balance the potential difference in a closed circuit. The ion diffusion occurs within the cell's interior, as Li ions are allowed to pass through the separator and eventually accept an electron once inserted into the anode. Please note that in this work, the term "lithiation" is used to indicate lithium intercalation in the carbon electrode, which occurs during the charging cycle.

2.4 Electrophoretic Deposition

Electrophoretic Deposition is a versatile technique employed to fabricate advanced Li-ion battery electrodes. In general, EPD works by applying an electric field to a suspension of charged particles, causing them to migrate and deposit onto a substrate of opposite charge. This process involves two main stages: electrophoresis, where charged particles move towards the electrode under the influence of the electric field, and deposition, where the particles accumulate and form a coherent film on the substrate.

In this specific application, EPD is used to deposit LFP particles combined with carbon black and reduced graphene oxide, with the assistance of cationic polymer (PDDA) in an ethanol suspension onto carbon fibre substrates. This method leverages the conductive and structural properties of CF, the high capacity and stability of LFP, and the conductive network formed by CB and rGO.

The preparation of a stable suspension is the first critical step in EPD. For LFP, CB, and rGO, ethanol is selected as the solvent due to its low viscosity and relatively high dielectric constant, promoting the dispersion of particles. PDDA acts

as a cationic polyelectrolyte, imparting a positive surface charge to the particles, facilitating uniform dispersion of LFP and rGO, which otherwise tend to aggregate due to van der Waals forces and π-π stacking interactions, respectively.[23,33]

The parameters of the EPD process, such as voltage, deposition time, and current density, are crucial in determining the quality of the deposited film. Typically, a constant voltage method is employed, where the applied voltage must be optimised to balance deposition rate and film quality. High voltages can increase the deposition rate but may lead to poor film quality due to rapid accumulation of particles, resulting in a less uniform and more porous structure. Conversely, lower voltages improve film quality but require longer deposition times. The distance between the electrodes influences the current density, affecting deposition kinetics and final film properties. A smaller electrode distance increases the electric field strength, enhancing the deposition rate but also risking higher local current densities, which can cause localised heating and affect film uniformity.[33]

Incorporating CB and rGO into the LFP matrix serves multiple functions. Both significantly enhance the electronic conductivity of the electrode, addressing the intrinsic low electronic conductivity of LFP (approximately 10^{-11} S/m). The conductive network formed by these carbon additives ensures efficient electron transport throughout the electrode, critical for high-rate performance and overall battery efficiency.[23,34]

CB provides ample conductive pathways and enhances the mechanical integrity of the electrode due to its high surface area. rGO, with its high conductivity and mechanical strength, improves electronic connectivity and contributes to structural stability. This combination ensures a synergistic effect, resulting in electrodes with superior electrochemical performance and durability.[33]

Optimising the concentration of LFP, CB, and rGO in the suspension is crucial for achieving balanced deposition. High concentrations of CB and rGO can improve conductivity but may lead to agglomeration, negatively impacting uniformity and adhesion of the film. Therefore, careful control of the suspension composition is essential to ensure a homogeneous and adherent coating. Additionally, the deposition time and applied voltage must be fine-tuned to achieve the desired film thickness and porosity. Prolonged deposition times can lead to thicker films, but with diminishing returns in terms of uniformity and mechanical stability. Excessive voltage can accelerate deposition but may compromise film quality due to cracks or voids[35].

The application of EPD for depositing LFP with CB, rGO, and PDDA on CF substrates offers a promising route to fabricate high-performance Li-ion battery electrodes. By carefully optimising the suspension stability, EPD parameters, and concentration of carbon additives, electrodes with enhanced electronic conductivity, structural integrity, and electrochemical performance can be produced. This method holds significant potential for the development of next-generation energy storage devices.

3

Materials and Methods

Experiment is the sole judge of scientific 'truth'."

— Richard P. Feynman

The "Materials and Methods" chapter serves as the cornerstone of this thesis, detailing the rigorous and methodical approaches employed to explore the innovative realm of structural battery technology. This chapter is designed to provide a transparent and reproducible framework for the experiments conducted, allowing for the clear presentation of methodologies that are foundational to the scientific process.

In the spirit of Richard Feynman's saying, each technique and material used in this study has been chosen not only for its relevance but also for its ability to provide precise and reliable data. From the initial selection of materials and their preparation through electrophoretic deposition and structural battery cell fabrication, to the comprehensive evaluation of their electrochemical performance and detailed material characterisation, each step has been carefully coordinated.

This chapter, therefore, not only documents the experimental journey but also underscores the scientific rigor involved in transforming theoretical concepts into empirical evidence that can advance the field of battery technology.

3.1 Investigated Materials

In this section, we describe the CFs used for electrode manufacturing and the preparation processes they underwent before coating. The primary focus of our research was on Pyrofil^{TM} HS40 12K carbon fibres, which we utilised for optimising the EPD process and for manufacturing the majority of the battery cells. For comparison purposes, we assembled several cells using HexTow^{TM} HM63 12K (Industrial) carbon fibres as the material for positive electrodes. In all cases, Torayca^{TM} T800S 12K were used as the material for negative electrodes. The general properties of the fibres used are listed in Table 3.1.

All CFs were spread by Oxeon AB, Sweden, to achieve a width of approximately 15 mm for T800S, 20 mm for HS40, and 17 mm for HM63. While T800S and HM63 fibres were used as received, the HS40 CFs underwent a cleaning process. Specifically, HS40 CFs were washed in DCM overnight using a Soxhlet extraction setup. For the purpose of comparison study, several samples have been desized using pyrolysis at 500 °C for 5 hours in air as well as using 65% nitric acid instead of DCM in the reflux setup for 2 hours. This pre-treatment was necessary because, unlike

Table 3.1. Typical mechanical properties of selected carbon fibres as per corresponding datasheets.

	HS40	**HM63**	**T800S**
Tensile Strength, MPa	4610	4344	5880
Tensile Modulus, GPa	425	435	294
Strain at Failure, %	1.1	1.0	2.0
Yield, mg/m	430	422	515
Density, g/cm^3	1.85	1.83	1.80

HM63, HS40 fibres are coated with a polymer sizing that can affect the fibre's performance in the EPD process and subsequent battery cell functionality[36]. This sizing, which can consist of epoxy or PU resin, is typically used to facilitate handling and enhance the bonding between the fibre and the matrix in composite manufacturing. For HM63, the absence of such a sizing layer and for T800S, the minimal impact of this sizing on the capacity when used as a negative electrode[37,38], led to the decision to use these fibres as received. This approach enhances the sustainability of the process by reducing unnecessary chemical treatments.

For the washing process, the CFs were cut into 7 cm long segments and sandwiched between two thin Teflon sheets measuring 2 cm in width and 7 cm in length. After washing, the fibres were spread using acetone to the desired width to ensure a uniform strip without gaps. This preparation was crucial for optimising the EPD process, as described in the subsequent section.

3.2 Methodology of Electrophoretic Deposition

In this study, EPD was utilised to coat carbon fibres with a cathode material composed of lithium iron phosphate blended with nanosheets of reduced graphene oxide and carbon black.

3.2.1 Coating Materials

For the EPD solution, we used LFP nanopowder (99.9% purity, APS 80-100 nm) from Nanoshel LLC, CB from Thermo Fisher Scientific Inc, and reduced graphene oxide (rGO, 95% carbon content) from LayerOne A/S, along with a 2% aqueous solution of PDDA from Sigma Aldrich. For the comparison purposes, we have also used microsized LFP powder from MTI Corporation (APS 3.5±1.5 μm) in several batches. The ethanol used was supplied by VWR Chemicals (99.9% purity).

3.2.2 EPD Recipes

The EPD solution was prepared using two distinct recipes:

1. **Recipe "2021":** Following the modified version of procedure described by Xia et al. (2024)[39], 450 mg of LFP was added to 50 ml of absolute ethanol. The mixture was sonicated for 10 minutes, followed by the addition of 450 microlitres of PDDA dissolved in 10 ml of absolute ethanol. After another

10 minutes of sonication, 25 mg of CB powder and 25 mg of rGO powder were added. The mixture was sonicated for an additional 20 minutes after using the remaining 10 ml of ethanol to clean any powder residues from the weighing plates.

2. **Recipe "2024":** Introduced by Dr. Richa Chaudhary in 2024, this method begins by mixing 450 mg of LFP with 25 mg of CB using a mortar and pestle, then dissolving the mixture in 50 ml of ethanol. After 10 minutes of sonication, 25 mg of rGO dissolved in 30 ml of ethanol was added, followed by another 10 minutes of sonication. Then, 450 microlitres of PDDA dissolved in 10 ml of absolute ethanol was added, and the remaining 10 ml of ethanol was used to clean any residues. The solution was sonicated for a final 20 minutes.

Both recipes are illustrated in the Figure 3.1.

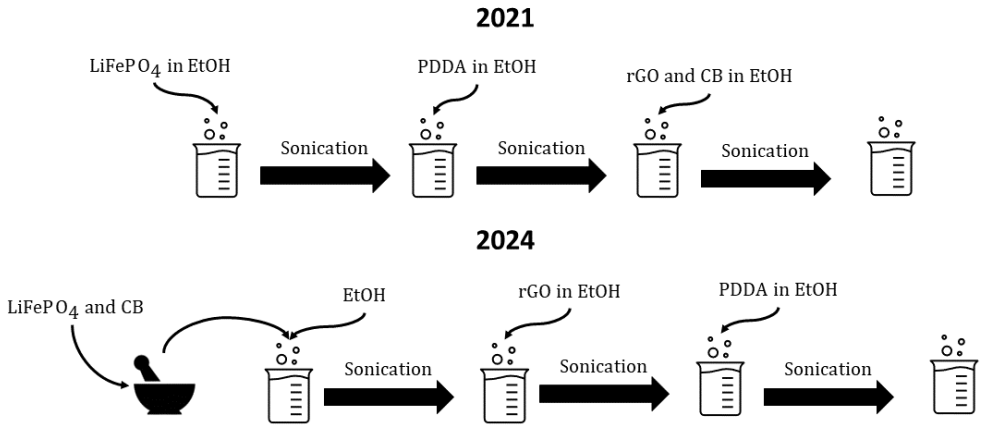

Figure 3.1. Schematic illustration of the two EPD recipes used for coating carbon fibres.

It should be noted that some batches used an incorrect sequence in the "2024" recipe by adding PDDA before rGO, marked by an asterisk near the recipe name in the experiments summary. Also, some solutions were used immediately after final sonication, while others were left overnight under stirring, sealed to prevent evaporation, and then sonicated for 20 minutes before EPD. Also it should be noted, that each sonication was performed using tip sonicator Sonics VCX-750 Vibra-Cell ultrasonic liquid processor. Each sonication was performed at 40% of tip amplitude which corresponds to 48 μm of excursion of the tip of the probe.

3.2.3 Sample Preparation for EPD

The preparation of the CF samples for the EPD involved several steps to ensure accuracy and repeatability in subsequent experiments. Initially, the washed CF were carefully positioned on 5 mm thick Teflon substrates. To secure them in place, copper tape was applied at the top and Kapton tape at the bottom. This arrangement was crucial for maintaining the alignment and orientation of the fibres during the EPD process.

To ensure precise quantification of the materials involved, the weight of each component was meticulously recorded. This included the Teflon substrate, the copper tape, and the Kapton tape. Additionally, the entire sample was weighed at various stages: before the EPD process, after EPD, and following a drying phase at 90°C. The coated fibres, still with both tapes attached, were also weighed. These measurements were essential for calculating the weight of the CF itself, the coating, and the active material, which in this case was lithium iron phosphate.

3.2.4 EPD Process

The EPD process was carried out with the following steps:

- The negative electrode was connected to the copper tape, and the positive electrode was connected to a platinum wire. A 3D-printed holder was used to ensure a constant distance of 2 cm between the electrodes.
- The assembly was dipped into the EPD solution, and an appropriate voltage was applied. Depending on the batch, either 5 or 7 samples were prepared from one batch of EPD solution, which was sonicated for half the duration of the EPD time between each sample preparation.
- A water bath with ice was used to maintain the ambient temperature of the solution during each sonication, using Sonics VCX-750 Vibra-Cell ultrasonic liquid processor.

In total, 22 EPD batches with 134 samples have been prepared throughout this thesis.

3.2.5 Direct vs. Stepwise EPD

Direct EPD involves applying a constant voltage throughout the deposition process, leading to a uniform film formation. Stepwise EPD, on the other hand, alternates between on and off steps of voltage application. This method can allow for better control over the film thickness and uniformity, as it gives particles time to settle and re-disperse, potentially reducing defects and improving the overall quality of the deposited layer. For instance, in this study, the "on" step duration was 2 minutes, followed by an "off" step of 1 minute. This stepwise method helps in managing the deposition rate and the internal stress of the deposited layers, thus potentially enhancing the adhesion and mechanical integrity of the coatings.

3.3 Structural Battery Cell Fabrication

The fabrication of structural battery cells requires a detailed assembly process using specialised materials in an inert and dry environment (inside the glove box at conditions less than 1 ppm O_2 and 1 ppm H_2O). These include glass sheets, pristine T800S carbon fibres for the negative electrode, copper and aluminium strips for current collectors, and a bespoke structural battery electrolyte, while the positive electrode utilises EPD-coated carbon fibre samples.

3.3.1 LE Preparation and Assembly Process

The liquid electrolyte is prepared by first heating ethylene carbonate on a heat plate to transition it from solid to liquid. This EC (99% anhydrous), sourced from Sigma Aldrich, is mixed in a 1:1 weight ratio with propylene carbonate (PC≥99%, acid<10 ppm, H_2O<10 ppm), also from Sigma Aldrich. Lithium salt (LiTFSI, 99.99%) is then added, with the proportion being 2.87 g per 10 ml of the EC:PC mixture.

For the assembly, carbon fibres are affixed to the current collectors using Pelco® Conductive Silver Paint for the negative electrode and Pelco® Conductive Carbon Glue for the positive electrode (both conductive adhesives are supplied by Ted Pella). Layers including a release plastic film, a Freudenberg separator (supplied by Freudenberg Performance Materials SE & Co) combined with a glass veil (6 g/m^2 supplied by Technical Fibre Products Ltd.), and a textile mesh for pressure distribution are sequentially stacked. For some cells, a Whatman glass microfiber separator (Whatman GF/A, 260 μm thick from Sigma Aldrich) is used, and several full cells and half cells are assembled without structural battery electrolyte, using only the liquid electrolyte.

Tacky tape secures the assembly's perimeter on the glass sheet, and two rubber pipes, only their ends surrounded by felt, protrude from the setup for subsequent steps. The assembly is sealed with an external plastic film and transferred to a glovebox for SBE preparation.

3.3.2 SBE Preparation, Infusion, and Curing

Inside the glovebox, under an inert atmosphere, the structural battery electrolyte is prepared. One rubber pipe is connected to a syringe filled with SBE, while the other is sealed to prevent air ingress and inhibit premature SBE curing. After preparation, the cell is removed from the glovebox for infusion, which is carried out at a pressure of -0.6 bar. Once the pressure is set, clamps are opened facilitating the start of the infusion process. At the end of infusion, clamps are closed (inlet first), and the cell upon detaching is cured in a furnace at 90 °C for 45 minutes.

Upon completion of the curing process, the cell is transferred back to the glovebox for final sealing. Each cell is placed into a pre-prepared pouch bag (PET:Al:PE, 12 μm:9 μm:75 μm thickness), sealed along the edges where current collectors touch with white and thermal tapes to ensure isolation. An extra 200 μl of LE is added to each side of the cell to assumingly improve ionic conductivity thus enhancing the cell's operational stability and efficiency.

3.3.3 Balancing Electrode Capacities and Half-Cell Preparation

During assembly, efforts are made to balance the capacities between the negative and positive electrodes. The amount of LFP on the positive electrode, which has a theoretical capacity of 170 mAh/g, dictates the required mass for the negative electrode, which possesses nearly double the capacity[37,40]. An additional 1 cm of electrode length is included to facilitate attachment to the current collector.

For half-cell configurations, precise measures are taken to align the components effectively. Lithium metal, cut to approximately match the size of the electrode, serves as the counter-electrode. Instead of glueing, the position of the Ni current collector is secured when the pouch bag is sealed, ensuring stability without permanent attachment to the lithium. The Whatman separator, utilised exclusively in half-cell assemblies, is wetted with 400 μl of LE during the packing of the constituents into the pouch bag. In contrast to full cells, only the positive electrode in half-cells is infused with the SBE.

3.4 Electrochemical performance evaluation

The assembled battery cells are rigorously tested using a Neware CT-4008-5V10mA-164 battery cycler for accurate control and data acquisition. This comprehensive evaluation includes cyclic voltammetry, galvanostatic charge-discharge, and electrochemical impedance spectroscopy.

Full cells undergo initial preconditioning through galvanostatic cycling at a C/40 charge rate for five complete charge/discharge cycles, based on the theoretical C-rate derived from the capacities of the LFP-coated positive electrode and its balanced negative counterpart. Subsequent cycling involves various C-rates (C/20, C/10, C/5, C/2, 1C, 2C, and back to C/10) for five cycles at each rate, with a two-minute rest between cycles to allow ion-concentration gradients to relax.

Following the cycling, EIS measurements are performed to assess the cells' impedance over a frequency range from 100 kHz to 100 mHz under alternating current. These tests are conducted before and after the cycling process to monitor changes in the electrochemical characteristics of the cells.

Selected full cells are subjected to long-term performance evaluations, undergoing 100 cycles of GCD at a C/10 rate to assess the durability of the structural battery composite. As for the half-cells, evaluations begin with cyclic voltammetry post-assembly. Similar to full cells, half-cells undergo cycling tests, in some cases without the initial conditioning step, based solely on the theoretical C-rate of the LFP-coated positive electrode. Similarly to the FCs, EIS is also performed on selected half-cells after GCD.

In total, 31 structural battery cells in various configurations were manufactured and characterised for their multifunctional performance.

3.5 Material characterisation techniques

3.5.1 Scanning Electron Microscopy

Scanning Electron Microscopy is a powerful technique we used to examine the detailed microstructure and surface morphology of materials at high magnification. This method was particularly crucial for analysing the surface features and the cross-sectional views of the electrode materials in our structural battery cells.

3.5.1.1 Sample Preparation

For the SEM analysis, we used the JEOL JSM-7800F Prime microscope. Using a scalpel we carefully cut out a segment from the middle of the positive electrodes, approximately 1 cm in length and 3-4 mm in width, which were coated using the EPD process. These samples were then directly mounted onto aluminium stubs using conductive carbon tape. To enhance the electron conductivity and improve the overall image quality, we sputter-coated the samples with a thin layer of gold using LeicaEM ACE600. This coating, around 5 nm thick, minimised charging effects and enhanced the clarity of our SEM images.

3.5.1.2 Imaging and Analysis

The SEM imaging allowed us to capture high-resolution surface topography and cross-sectional views of the samples. By taking high-magnification images, we could examine the uniformity of the LFP and carbonaceous materials coating the carbon fibres. This analysis helped us identify any microstructural irregularities and understand their potential impact on the battery cells' performance.

Analysing the cross-sections of the coated fibres, we measured the coating thickness and inspected the interface between the active material and the carbon fibres. These insights are vital for understanding how the structural features of the coatings contribute to the electrodes' mechanical and electrochemical properties.

3.5.2 Sheet Resistance Measurement

In our material characterisation efforts, we measured the sheet resistance of coated positive electrodes and pristine CFs HS40 to evaluate their electrical properties for use in structural batteries. The method applied was direct and focused on the functional attributes of the samples post-manufacturing.

The coated positive electrodes used in the experiments retained the copper tape on the top and Kapton tape on the bottom, which were applied prior to the EPD process. For the resistance measurement, each electrode was placed on a glass substrate to ensure an insulated backing that would not influence the results. The measurements were performed using the EverBeing SR-4-6L Four-Point Prober. This instrument is adept at providing accurate resistance readings by minimising the impact of contact resistance, which is crucial for assessing the uniformity and effectiveness of the conductive coatings on the electrodes.

Resistance was specifically measured at the middle of the sample, 1 cm away from the Kapton tape, to avoid edge effects and to assess the most representative part of the electrode. A low voltage of 1 mV was used during these measurements to avoid altering the material properties through electrical stress.

Similarly, the pristine CFs HS40 underwent resistance measurement to serve as a baseline for comparison with the coated electrodes. This comparison is vital for understanding the impact of the EPD coating on the electrical conductivity of the fibres.

4

Results and Discussion

"If we knew what we were doing, it would not be called research, would it?"
— Albert Einstein

The insightful observation by Albert Einstein captures the essence of the exploratory journey undertaken in this thesis. The Results and Discussion chapter is where we delve into the complexities and uncertainties of the experimental outcomes, reflecting on both expected and unexpected findings that have surfaced through our rigorous investigative processes.

The discussion begins with an examination of the EPD process, where different desizing methods are evaluated for their effectiveness. The results from EPD are analysed, particularly focusing on the influence of time on self-assembly and the impact of various solution recipes. The comparative study extends to exploring the differences between stepwise and direct EPD methods and between the use of micro-sized and nano-sized lithium iron phosphate.

Moving into the realm of electrochemical performance, the chapter presents data from cycling tests and electrochemical impedance spectroscopy for both half-cells and full-cells as well as cyclic voltammetry results for the half-cells. Despite preparing 31 cells, only 10 provided usable data, highlighting the inherent challenges and unpredictability of experimental science.

Finally, the discussion touches on the measurements of shear resistance conducted on selected samples. As we navigate through these sections, we aim to draw meaningful conclusions from the data, proposing explanations for the observed behaviors and identifying areas for further investigation.

4.1 Part I - Positive Electrodes Manufacturing

4.1.1 Desizing Methods

This subsection presents SEM images of desized HS40 CFs treated through various methods. Due to the manufacturing secret nature of sizing compositions, identifying the most effective desizing methods is crucial for optimal CF functionalisation during EPD.

Desized HS40 samples were compared after treatments including refluxing in dichloromethane overnight (Figure 4.1c), in 65% nitric acid for several hours (Figure 4.1d), and pyrolysis at 500 °C for 5 hours (Figure 4.1b) in an oxygen atmosphere.

Pyrolysis, while effectively removing sizing, caused extensive surface damage. In the future, lower temperatures, inert atmosphere, or shorter exposure times can be used to mitigate such effects.

Samples treated with DCM overnight (Figure 4.1c) and nitric acid (Figure 4.1d) exhibited mediocre results, retaining prominent features (bright lines) of sizing similar to untreated HS40 CFs (Figure 4.1a).

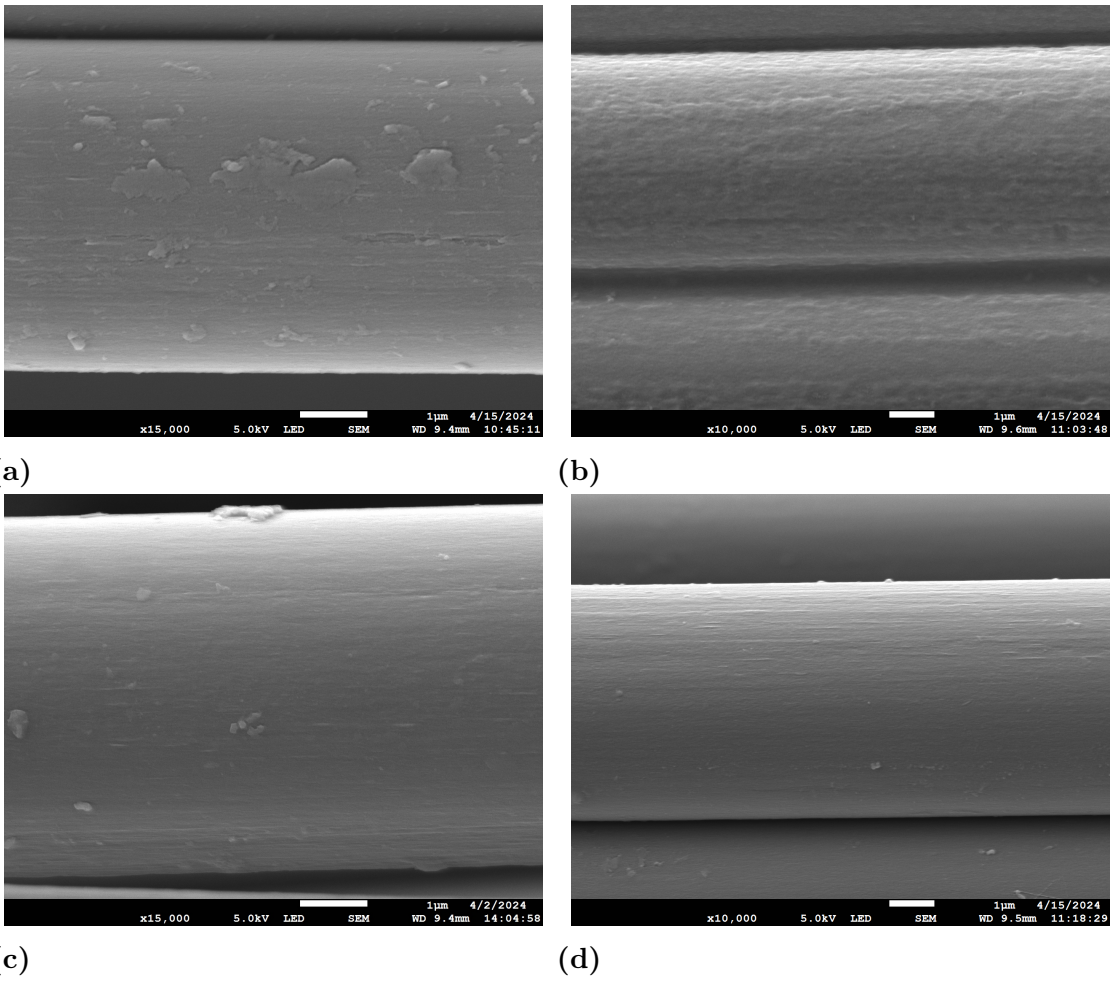

(a) **(b)**

(c) **(d)**

Figure 4.1. SEM images of desized HS40 CFs: **a)** sized CFs; **b)** pyrolysis at 500 °C for 5 hours in air; **c)** reflux in DCM overnight; **d)** reflux in 65% nitric acid for several hours.

It should be noted, that distinct bright agglomerates are gold particles originating from the sample preparation.

4.1.2 CFs functionalisation results

Functionalisation of DCM desized HS40 CFs with $LiFePO_4$/CB/rGO coating was achieved using EPD. Given the sensitivity of this method, the first goal was to define optimal parameters for the desired cathode coating. The optimal parameters for cathode coating aimed for a deposit loading of approximately 5-6 mg/cm^2, resulting

in a total mass of about 30 mg for samples with area 4.0x1.5 cm^2. These deposit loading values were initially derived from prior studies on all-fibre working cells.

Generally, the deposited material volume increased with longer deposition times. Optimal mass loads were attained by varying voltage and time, with parameters ranging from 70-80 V over 10 to 20 minutes, as detailed in Table 4.1.

Table 4.1. Active material mass (nano-LFP, mg) obtained with different voltage-time conditions during EPD. This table contains batches varied by recipes and self-assembly duration. The table aims to provide insights into the effects of time and voltage combinations on coating mass.
* The batch produced without a holder that ensures a fixed distance between electrodes.

No.	70 V/20 min	70 V/15 min	70 V/10 min*	80 V/10 min	80 V/7 min	80 V/5 min
1	19.46	18.05	11.20	18.64	12.51	11.77
2	26.58	31.35	17.54	24.88	26.32	15.20
3	35.97	21.52	14.31	23.52	14.94	9.96
4	26.55	28.90	15.35	30.36	18.32	10.15
5	22.77	25.93	9.29	28.67	14.72	13.95
6	20.97	17.38	11.52	-	13.78	-
7	18.15	18.97	7.16	-	14.12	-
Average	**24.35**	**23.16**	**12.34**	**25.21**	**16.39**	**12.20**

Moreover, the influence of different voltage-time combinations on mass gains and electrochemical properties was assessed. For example, the 70 V/20 min and 80 V/10 min batches (Table 4.1) exhibited negligible differences, as did the batches of 70 V/10 min and 80 V/5 min. Additionally, the results are confirmed with another series of depositions performed with full pre-conditional alignment (Table 4.2). The Least Significant Difference method affirmed that the differences between 80 V/10 min and 70 V/20 min deposition conditions are not statistically significant at a 99% confidence level.

Given that the coating masses for the voltage-time pairs (such as 70 V/20 min and 80 V/10 min; 70 V/10 min and 80 V/5 min) are nearly identical (Table 4.1), regardless of the recipes used and the duration of self-assembly, we next evaluated the electrochemical performance of comparable samples using SEM surface analyses. The microstructure of the samples, which shared similar coating masses and were based on the same suspension recipe ("2021, fresh"), was examined under SEM. The cross-sections of two samples prepared under 80 V/10 min and 70 V/20 min deposition conditions revealed no significant differences, with both samples featuring areas of high and low loading (Figures 4.2). High-loading areas in cathodes heavily impregnated with active material (Figures 4.2c,d), are presumed to enhance battery cell performance by increasing the capacity of the active material. However, this may also lead to potential ion transfer blockages due to the increased volume of material. Therefore, it is impractical to rely solely on a large total active material mass. Thus, we can conclude that samples produced under 80 V/10 min and 70 V/20 min deposition conditions likely exhibit similar electrochemical properties.

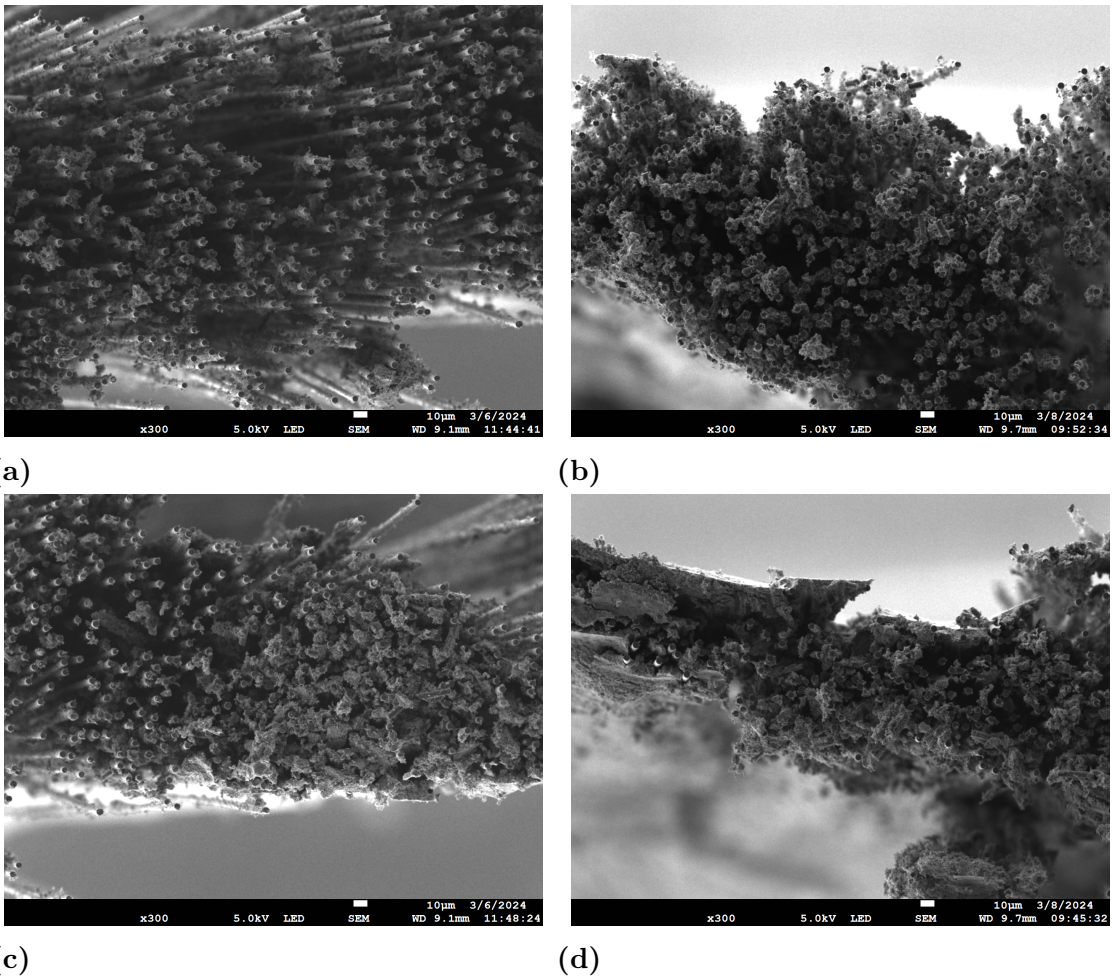

(a) **(b)**

(c) **(d)**

Figure 4.2. Cross-sectional SEM images of nano-LFP based coatings on samples prepared at 80 V/10 min and 70 V/20 min, respectively: **a)** and **c**) for the 30.58 mg sample; **b)** and **d**) for the 35.97 mg sample. These samples were prepared using the "2021" recipe with fresh suspensions.

Table 4.2. Masses of active material deposited using 70 V/20 min and 80 V/10 min EPD parameters. Both EPD solutions (nano-LFP) were prepared per the "2024" recipe and stirred overnight.

Active material (LFP), mg		
No.	**80 V/10 min**	**70 V/20 min**
1	17.22	29.74
2	34.66	39.91
3	33.13	25.37
4	34.55	32.33
5	27.13	18.08
6	15.97	24.47
7	17.59	19.29
Average	**25.75**	**27.03**

4.1.3 Self-assembly Duration Time Effects

Prior to coating deposition, rGO, and CB must combine with $LiFePO_4$ to form a non-agglomerating, well-dispersed LFP suspension, which is essential for uniform coatings. We anticipated that electrostatically induced self-assembly would require time to stabilise the nano-particle system. The literature lacks specific timescales for this phase of solution preparation and the materials we use. Therefore, coating deposition was investigated with the self-assembly timescale in mind as a part of the EPD suspension preparation.

Table 4.3 shows that overnight-stirred solutions provide more stable mass distributions than freshly used solutions post-sonication. While average mass values are similar (the differences are not statistically significant at a 99% confidence level), reliance on these alone is infeasible due to ethanol evaporation during EPD altering active material concentrations, which in turn leads to samples' mass variations being strongly dependent on the deposition order.

Table 4.3. Masses of active material deposited at 80 V for 10 min and 5 min. Solutions were prepared using the "2024" recipe with nano-LFP active material, highlighting the effects of the overnight-stirred (aged) and freshly prepared (fresh) solutions on particles' self-assembly time, and subsequently on coating's mass loading and distribution within the batch.

Active material (LFP), mg				
No.	**80 V/10 min**		**80 V/5 min**	
	Fresh	**Aged**	**Fresh**	**Aged**
1	26.53	17.22	17.36	11.77
2	43.21	34.66	12.09	15.20
3	16.18	33.13	14.89	9.96
4	23.93	34.55	14.35	10.15
5	21.87	27.13	6.94	13.95
6	22.34	15.97	10.28	-
7	8.85	17.59	10.47	-
Average	**23.27**	**25.75**	**12.34**	**12.20**

4.1.4 Solution Recipes' Comparison

Table 4.4 shows no significant difference in average mass gain between the "2021" and "2024" solution recipes for the cathode coatings deposited both in fresh solutions. However, the "2024" recipe notably deviates in mass distribution across deposition orders.

Table 4.4. Masses of active material (nano-LFP) deposited using direct EPD and fresh solution at 80 V/10 min, illustrating the influence of different recipes on coating mass loading and distribution within the batch.

Active material (LFP), mg		
No.	**"2021"**	**"2024"**
1	30.12	26.53
2	30.58	43.21
3	20.07	16.18
4	27.54	23.93
5	21.68	21.87
6	17.51	22.34
7	19.98	8.85
Average	**23.93**	**23.27**

Although the "2021" recipe appears advantageous based on table data, cross-sectional and planar SEM images (Figure 4.3) indicate that the "2024" recipe may deliver comparable electrochemical performance to cathodes prepared per "2021" recipe. The "2024" sample with the highest coating mass, 43.21 mg (Figure 4.3a) has much less empty space in the planar view between surface CFs compared to the planar view of the most loaded sample of "2021" recipe batch, having 30.58 mg of LFP (Figure 4.3b). Within the CF tow, cross-sectional micrographs demonstrate that the "2024" recipe maintains consistent spacing between CFs (Figure 4.3c) in comparison to the "2021" sample, which has both high and low loaded areas (Figure 4.3d). Additionally, a prominent wall of active material has formed on the facet of the "2024" sample, which was facing the counter electrode during EPD (Figure 4.3c). The consistent empty-spaced "2024" sample implies a promising cathode for electrochemical performance as it means that SBE is capable of full encapsulation of each carbon fibre within the tow, facilitating ion transfer. However, the anticipated performance might be disrupted by the wall of coating formed on one side. Taking into account all these advantages and drawbacks we can conclude that both recipes, "2024" and "2021" hold equal promise as effective preparation for cathodic material for battery cells. Additional studies should be made to state what properties would facilitate the electrochemical performance the most.

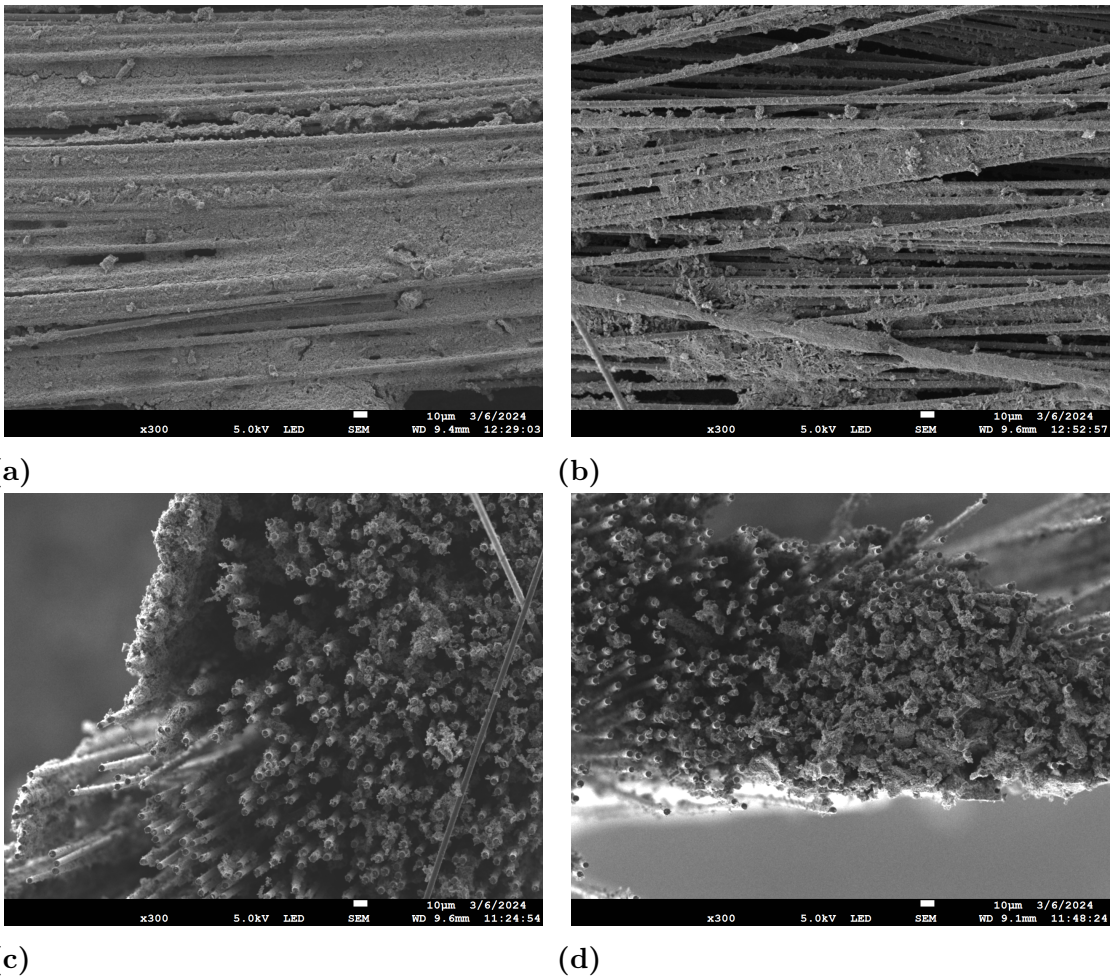

Figure 4.3. SEM images comparing "2024" and "2021" EPD recipe (nano-LFP) samples under fresh solution conditions at 80 V/10 min: **a)** "2024" recipe, planar view, mass loading 43.21 mg; **b)** "2021" recipe, planar view, mass loading 30.58 mg; **c)** cross-section of "2024" recipe sample; **d)** cross-section of "2021" recipe sample.

4.1.5 Direct and Stepwise EPD

According to the Table 4.5, the mass distribution is significantly more stable in stepwise deposition than in direct deposition. Samples exhibiting closely comparable mass gains were analysed using SEM. Cross-sectional SEM images reveal that samples prepared via direct deposition demonstrate greater infiltration of cathodic material within the bulk of the CF tow (Figure 4.4c). In contrast, stepwise deposition tends to create a distinct coating on the forefront of the CF tow, leaving the interior with considerably more empty space (Figure 4.4d). However, planar SEM images show no notable differences between the samples (Figures 4.4a and 4.4b).

Table 4.5. Masses of active material (nano-LFP) deposited using "2021" fresh solution for direct and stepwise EPD at 80 V/10 min. For stepwise deposition, the "on" step duration is 2 min, and the "off" step is 1 min.

Active material (LFP), mg		
No.	**Direct**	**Stepwise**
1	30.12	11.50
2	30.58	12.32
3	20.07	22.28
4	27.54	18.49
5	21.68	19.40
6	17.51	15.14
7	19.98	15.68
Average	**23.93**	**16.40**

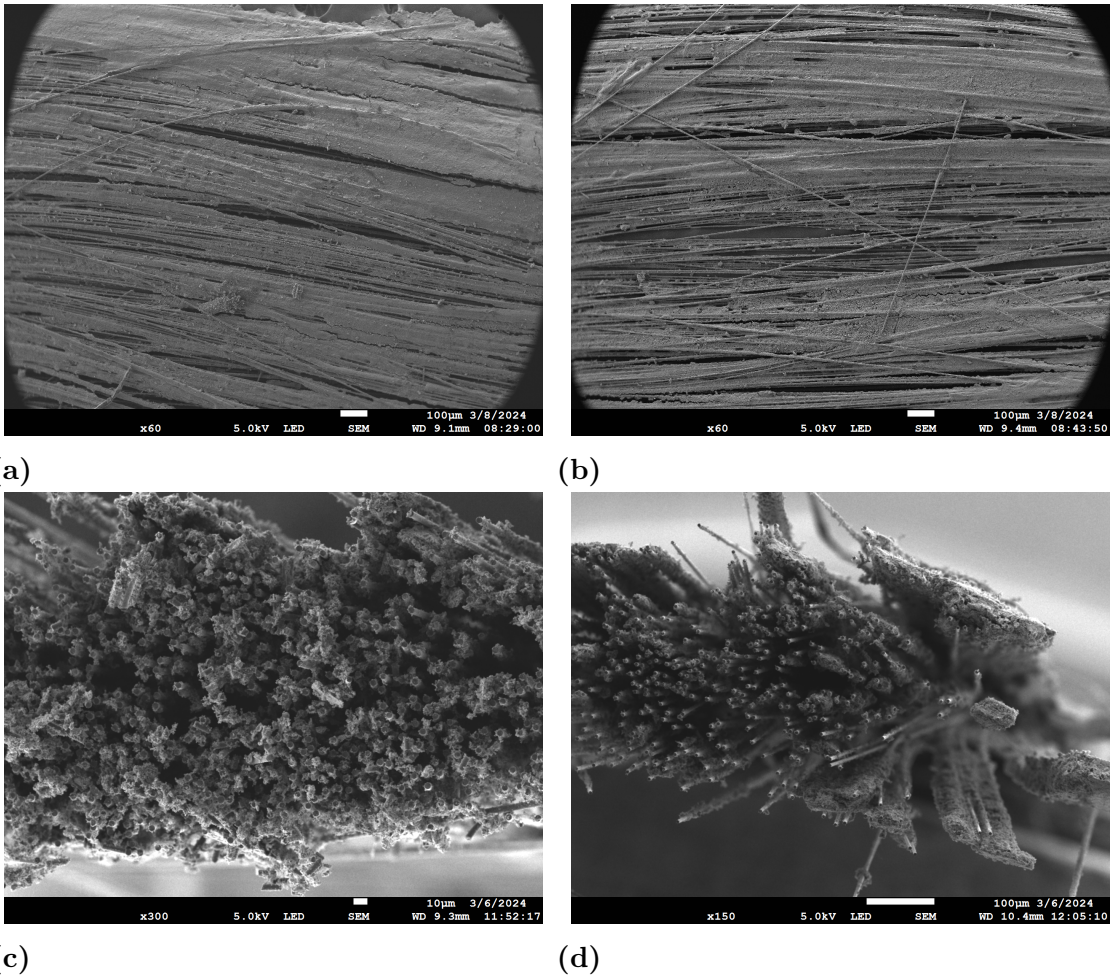

(a) **(b)**

(c) **(d)**

Figure 4.4. SEM images comparing nano-LFP coatings deposited by direct and stepwise EPD both for 80 V/10 min: **a)** direct EPD, planar view, 3.19 mg/cm^2; **b)** stepwise EPD, planar view, 3.38 mg/cm^2; **c)** direct EPD, cross-section; **d)** stepwise EPD, cross-section.

4.1.6 Micro- and Nano-LFP

The deposition results for micro and nano-LFP, presented in Table 4.6, show similar patterns. The standard deviations for micro- and nano-LFP batches are 2.94 mg and 3.22 mg respectively, indicating comparable variance, as well as average values and mass gains for each type. SEM micrographs (Figure 4.5) of the micro-LFP sample display typical coverage corresponding to an active material mass of 15.17 mg.

Table 4.6. Masses of active material deposited on 24k fibre samples at 80 V for 5 minutes using freshly prepared solutions from the "2024" recipe, comparing micro-LFP and nano-LFP.

Active material (LFP), mg		
No.	**80 V/5 min, micro-LFP**	**80 V/5 min, nano-LFP**
1	16.19	17.36
2	10.16	12.09
3	15.17	14.89
4	13.10	14.35
5	9.56	6.94
6	-	10.28
7	-	10.47
Average	**12.83**	**12.34**

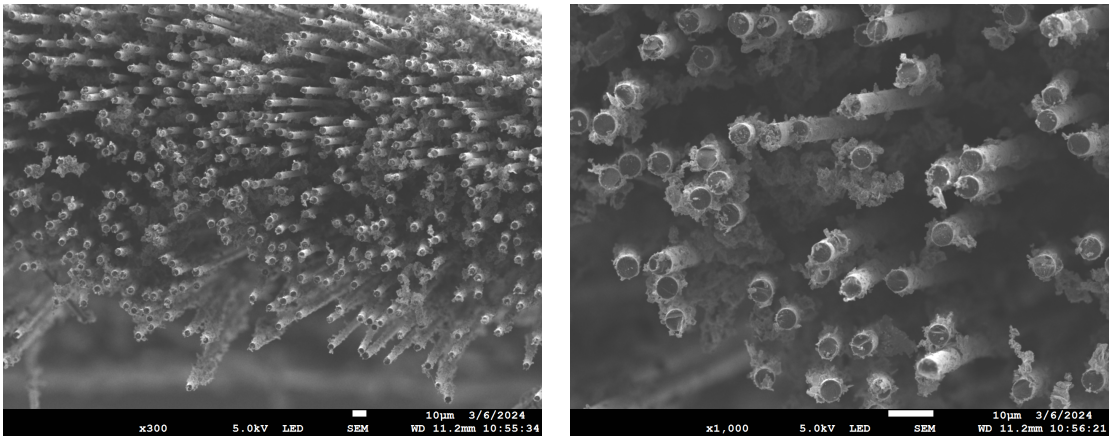

(a) **(b)**

Figure 4.5. SEM micrographs of a 15.17 mg cross-section sample coated with micro-LFP at 80 V for 5 minutes using a fresh solution prepared per the "2024" recipe; the sample contains 24k fibres. The images were captured at a single site: **a)** at 300x magnification; **b)** at 1000x magnification.

4.2 Part II - Electrochemical performance

Tables 4.8 and 4.7 present gathered data of the coated electrodes utilised further as a cathode for fully operational full and half-cells, respectively.

Table 4.7. Parameters of half-cells, including active material mass (LFP), EPD parameters, recipe, and separator used. Each half-cell has been prepared using positive electrodes with nano-sized LFP. Asterisk denotes wrong sequence of the "2024" recipe, where PDDA is added as the second step instead of last.

Sample #HS40	LFP, mg	EPD parameters	EPD recipe	Separator
MK67	19.40	80 V/10 min, stepwise	2021, fresh	Freudenberg, glass veil
MK104	24.50	80 V/10 min, direct	2024*, overnight	Whatman
MK105	28.78	80 V/10 min, direct	2024*, overnight	Whatman
MK118	34.99	80 V/10 min, direct	2024*, overnight	Whatman
MK119	23.47	80V/15min, direct	2024*, overnight	Whatman

Table 4.8. Parameters of full cells, including active material mass (LFP), EPD parameters, recipe, and separator used. Note that MK35 uses micro-LFP positive electrode unlike the other samples that use nano-LFP ones. Asterisk denotes wrong sequence of the "2024" recipe, where PDDA is added as the second step instead of last.

Sample #HS40	LFP, mg	EPD parameters	EPD recipe	Separator
MK100	23.97	80 V/10 min, direct	2024*, overnight	Freudenberg, glass veil
MK107	20.83	80 V/10 min, direct	2024*, overnight	Freudenberg, glass veil
MK52	23.93	80 V/10 min, direct	2024, fresh	Whatman
MK27	13.10	80V/5min, direct	2024, fresh	Whatman
MK35	12.09	80V/5min, direct	2024, fresh	Whatman

4.2.1 Half-cells

The electrochemical performance of the half-cell with an MK67 positive electrode is presented in Figure 4.6. Figure 4.6a shows the second charging and discharging cycles at various current rates with the characteristic of SB voltage profiles. The battery, with a positive electrode mass loading of 19.40 mg, functions effectively up to a C/2 current rate (the battery is charged and discharged in 2 hours). However, at higher rates, the initial discharge voltage is lower and drops much steeper. Such behaviour is often referred to as the voltage sag, which typically occurs under increased internal resistance at higher discharge rates.

Despite these drawbacks, the half-cell fully recovered its capacity at slower rates, achieving approximately 70 mAh/g, almost identical to the initial C/10 rate, after cycling through all tested current rates. As expected, specific capacity diminishes at higher C-rates, reflecting the reduced energy extractable under rapid discharge conditions.

According to the manufacturer, the nominal capacity of the LFP is 170 mAh/g. At a relatively fast current rate of C/10, the discharging capacity of the half-cell approaches 70 mAh/g, meaning that around 40% of the material was utilised, whereas

at C/40 rate the capacity remains at a higher value – 65%. However, these capacity retention values are considered high, and it is attributed to the use of lithium metal as a counter electrode, which prevents irreversible Li-ion intercalation, unlike carbon fibres.

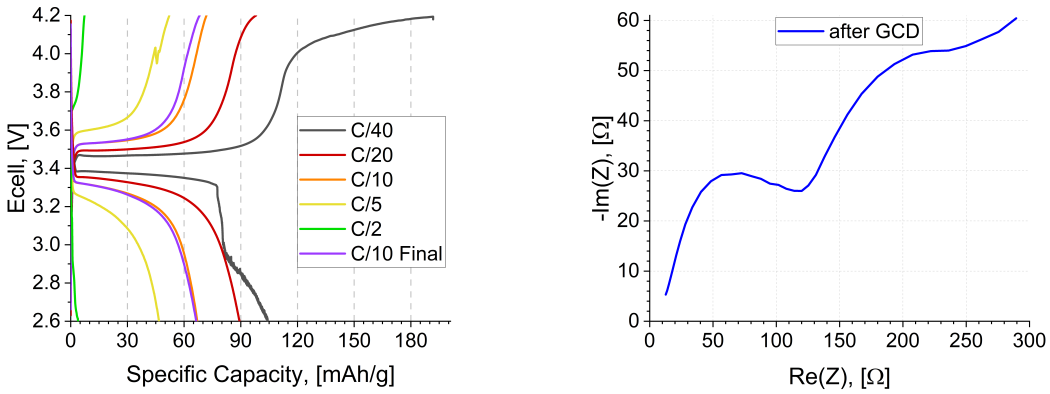

(a) MK67 (19.40 mg; 3.08 mg/cm^2), GCD **(b)** MK67 (19.40 mg; 3.08 mg/cm^2), EIS

Figure 4.6. GCD and EIS data for the MK67 half-cell; 80 V/10 min (Table 4.7).

The Nyquist plot after GCD cycles, shown in Figure 4.6b, exhibits a typical battery impedance profile. According to the plot the bulk resistance of the half-cell, encompassing the electrodes, electrolyte, and separator, is approximately 12.7 Ω. The first semicircle in the high-frequency region indicates charge transfer resistance, ranging from 13 to 120 Ω, which significantly influences the half-cell's power density. This resistance is related to ion movement across the electrode-electrolyte interface and varies with the surface coating and particle sizes. Generally, the lower and more defined semicircle is the better the battery performance. The "tail" in the low-frequency region, indicative of Warburg Impedance, reflects the diffusional effects of Li-ions in the electrolyte, and through the host material. The slope is indicative of efficiency and capacity during charge-discharge cycles. Thus, in the case of MK67 half-cell, a gentle slope suggests slow ion diffusion.

In Figure 4.7 GCD profiles are demonstrated for four distinct half-cells containing MK104, MK105, MK118, and MK119 positive electrodes, with varying amounts of LFP. These profiles display trends similar to those in Figure 4.6a. Notably, the MK104 half-cell (Figure 4.7a) exhibits a discharge specific capacity of approximately 105 mAh/g at a C/20 rate, comparable to that of MK67, despite having approximately 25% higher active material mass. Furthermore, cells MK104, MK105 (Figure 4.7b), and MK119 (Figure 4.7d) demonstrate a slower decrease in specific capacity with increasing current rates compared to MK118 (Figure 4.7c), which has a significantly higher LFP loading (5.47 mg/cm^2 or 34.99 mg) resulting in almost half of the maximum specific capacity of the MK104.

The GCD performance of MK104, MK105, and MK119 is consistent, sharing the same EPD parameters and recipes, contrasting with the MK67 sample which used a fresh solution based on the "2021" recipe and stepwise deposition. From this, we may conclude that direct deposition at 80 V/10 min using a "2024" recipe of the overnight stirred solution, and a final mass load of at least 3 mg/cm^2 produces

cathodes yielding half-cells with higher performance. This suggests that direct deposition at 80 V/10 min with a "2024" recipe (even with the wrong sequence) and overnight solution stirring might also result in more effective full-cell performance. This improvement could stem from enhanced CB and LFP particle integration via crushing, which improves conductivity and simplifies the self-assembly process, as the former lasts longer, it leads to the better stability of assembled particles.

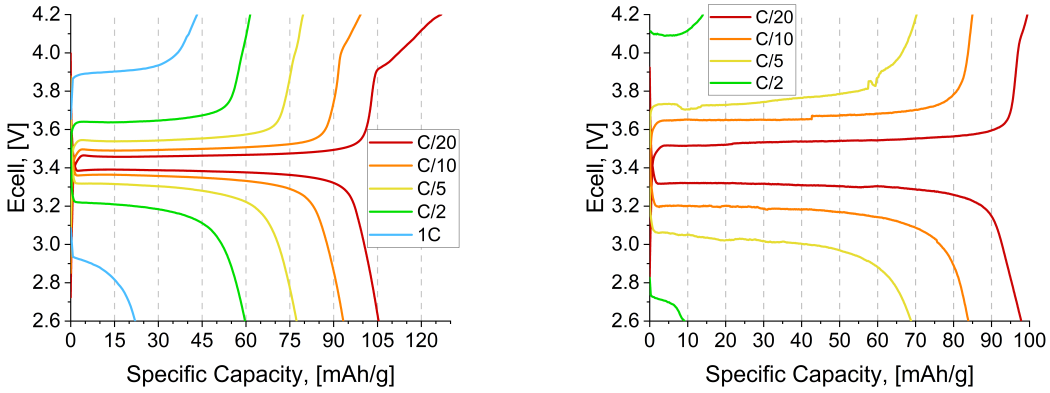

(a) MK104 (24.50 mg; 3.31 mg/cm^2), GCD. **(b)** MK105 (28.78 mg; 4.23 mg/cm^2), GCD.

(c) MK118 (34.99 mg; 5.47 mg/cm^2), GCD. **(d)** MK119 (23.47 mg; 4.01 mg/cm^2), GCD.

Figure 4.7. Comparison of GCD data for various half-cells; EPD parameters are 80 V/10 min for all samples except MK119 for which it is 80 V/15 min as stated per the Table 4.7. All the half-cells contain SBE, except MK119, which is solely liquid electrolyte half-cell.

Notably, MK104 is one of two half-cells that maintain a non-zero discharge capacity at a 1C rate. Considering its highest discharge capacity, it establishes a mass load of 3.31 mg/cm^2 as the most effective for half-cell performance with nano-sized LFP. Interestingly, the least effective half-cell (MK118) in terms of capacity and the most effective half-cell (MK104) are the only SBE-cured half-cells that managed to perform well under high current, up to 1C rate. Moreover, only the least effective cell, among all the 3 cells cured with SBE, managed to fully recover after high-rate discharge (Figure 4.7c). The GCD plot presented in Figure 4.7d corresponds to the half-cell containing solely liquid electrolyte. Despite SBE absence in this half-cell,

the values of discharge capacities at various current rates do not differ significantly in comparison to the corresponding values of SBE-cured half-cells.

The GCD plot in Figure 4.7d represents a half-cell based on a liquid electrolyte, which serves as a reference half-cell. Notably, despite lacking SBE, the discharge capacities at various current rates closely match those observed in half-cells with SBE.

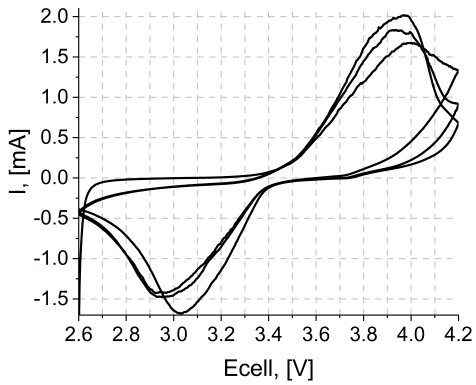

(a) MK104 (24.50 mg; 3.31 mg/cm^2), CV.

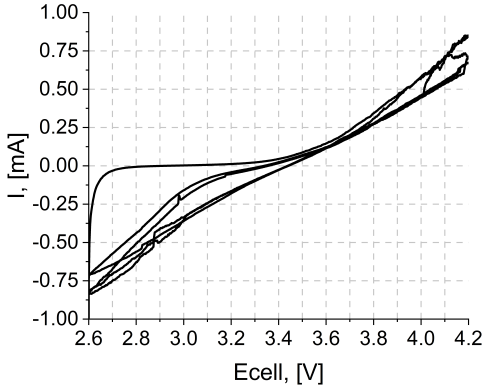

(b) MK105 (28.78 mg; 4.23 mg/cm^2), CV.

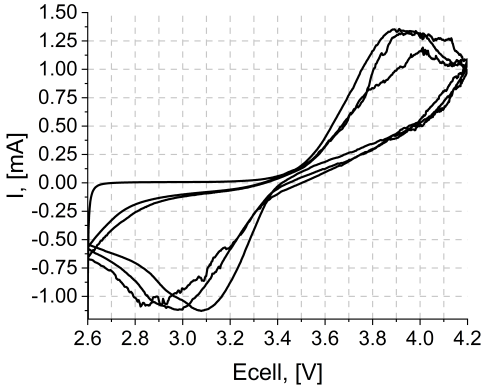

(c) MK118 (34.99 mg; 5.47 mg/cm^2), CV.

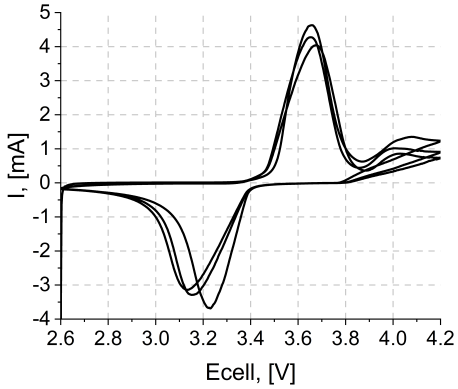

(d) MK119 (23.47 mg; 4.01 mg/cm^2), CV.

Figure 4.8. Comparison of CV data for various half cells; EPD parameters are 80 V/10 min for all samples except MK119 for which it is 80 V/15 min as stated per the Table 4.7.

Figure 4.8 displays CV peaks for the oxidation/reduction reactions of Fe^{2+}/Fe^{3+} in LFP particles[23]. The potential differences between the redox peaks for MK104 and MK118 are approximately 0.9 V, indicating high polarisation and limited ion transfer compared to previous studies[23]. Although the charge transfer resistance measured after cyclic voltammetry is twice as high for MK118 (Figure 4.9a) compared to MK119, which uses only liquid electrolyte (Figure 4.9b), MK118 achieves operational status at higher current rates. This occurs despite its lower reversibility indicated by CV profiles and high LFP loading. This discrepancy might stem from the significant increase in charge transfer resistance observed in MK119 after GCD cycling. Conversely, the half-cell with liquid electrolyte demonstrates typical CV

profiles (Figure 4.8d) with a smaller potential difference of 0.5 V between sharp and highly symmetrical peaks.

MK105 (Figure 4.8b) shows broad, subdued peaks, indicative of slower reaction rates and higher resistance. Notable shape changes through cycling may result from side reactions or material degradation. The comparison between the cell exhibiting the highest capacitance (Figure 4.8a) and the one with extremely high loading (Figure 4.8c) shows that both have relatively smooth and overlapping curves, which suggests stable electrochemical reactions, good reversibility, and balanced distribution of active material within the half-cells.

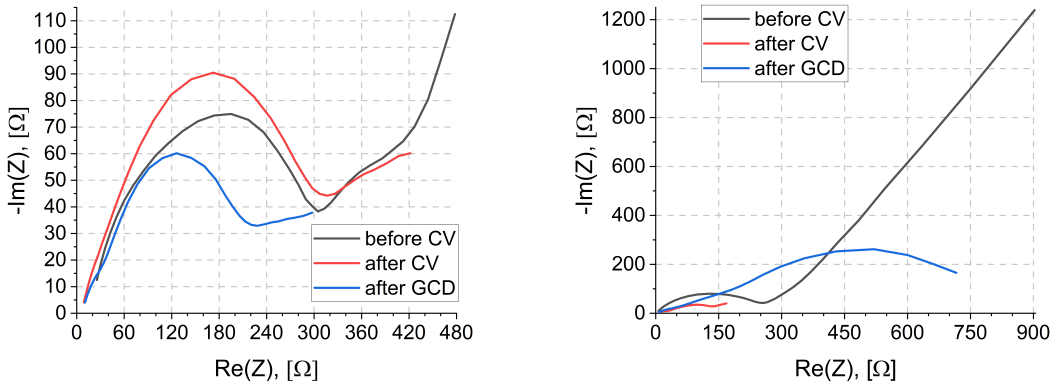

(a) MK118 (34.99 mg; 5.47 mg/cm^2), EIS. **(b)** MK119 (23.47 mg; 4.01 mg/cm^2), EIS.

Figure 4.9. Comparison of EIS data for two half cells at different stages of characterisation as per the Table 4.7.

4.2.2 Full cells

Figure 4.10a demonstrates typical voltage profiles seen for the half-cells, however with a much lower specific capacity and much more pronounced voltage sag. At C/40, specific capacity is the highest, roughly 17 mAh/g, while at C/10, the capacity drops to 6 mAh/g. Notably, the final C/10 cycle shows capacity retention even higher than the initial, indicating good recovery and stability of the electrode materials. Figure 4.10c illustrates the plot of the specific capacity change over 100 cycles at a constant C/10 rate. The capacity increases initially, reaching a peak around 7.8 mAh/g, before gradually decreasing with further cycling. The curve indicates the full cell's retention over 100 cycles of 75%, which is a moderate degradation for SB for 100 cycles.

Figure 4.10d shows the energy density for a cell at different C-rates. A significant capacity fade is identified, reflecting poor stability of energy densities at the studied C-rates. The energy density during discharge is consistently lower than during charge, except for the C/20 current rate, indicating significant energy losses. Based on the impedance measurements presented in Figure 4.10b this might be attributed to large charge-transfer resistance or other possible inefficiencies in the cell.

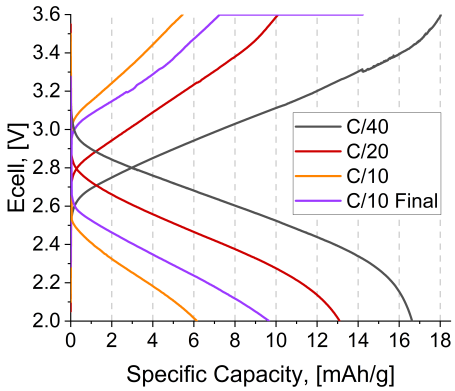

(a) GCD at different C-rates.

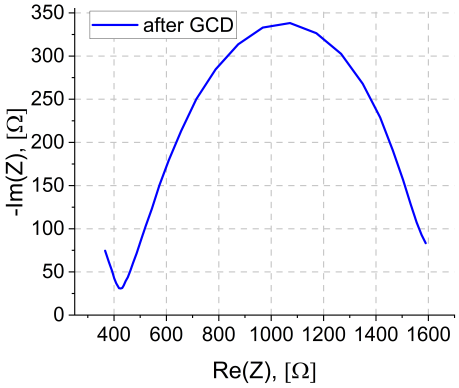

(b) EIS measurements.

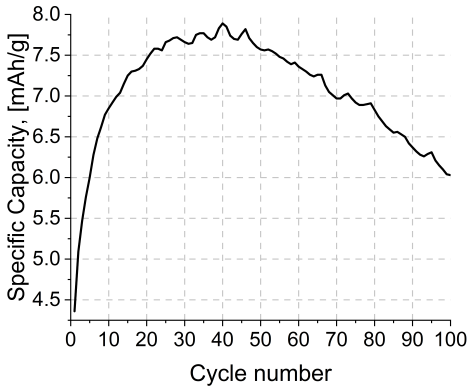

(c) Long term cycling at C/10 rate.

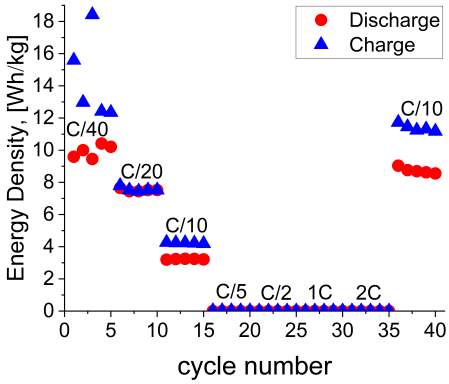

(d) Energy density at different C-rates.

Figure 4.10. Plots of GCD **(a)**, EIS **(b)**, long-term cycling **(c)** and energy density **(d)** data for MK107 (20.83 mg LFP; 3.18 mg/cm^2; 80 V/10 min) at different stages of characterisation as per the Table 4.8.

The other two full cells, MK100 (Figure 4.11a) and MK52 (Figure 4.11c), with highly similar active material masses, exhibit typical decreases in specific capacity with increasing C-rates, as previously shown. Despite having similar LFP coating masses, the reference full cell MK52 shows higher performance and greater capacities, which can be attributed to the absence of SBE.

Notably, full cells containing Freudenberg separators (MK107, MK100) exhibit very similar capacity and recovery behaviour, maintaining consistent performance up to the C/10 current rate, regardless of the implementation of negative electrode balance (MK107). Additionally, the MK100 demonstrated results consistent with MK107, surpassing the initial discharge capacity at a C/10 rate. (Figure 4.11a). Both cells — MK107 and MK100 — demonstrate up to a tenfold increase in charge transfer resistance after GCD compared to MK52, which is reflected in MK52's higher performance. Significant voltage sags are observed in these full cells, indicating challenges in overcoming internal resistance from the outset. However, the bulk resistance for MK52 (Figure 4.11d) and MK100 (Figure 4.11b) remains low, showing no drastic changes after GCD cycling.

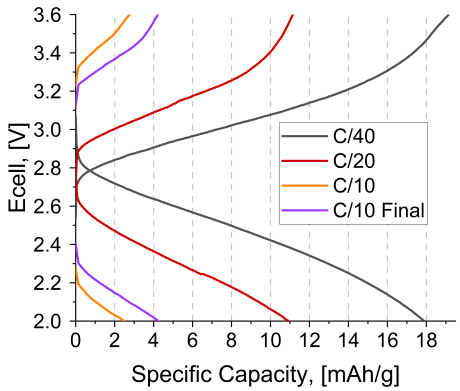

(a) MK100 (23.97 mg; 3.17 mg/cm^2), GCD.

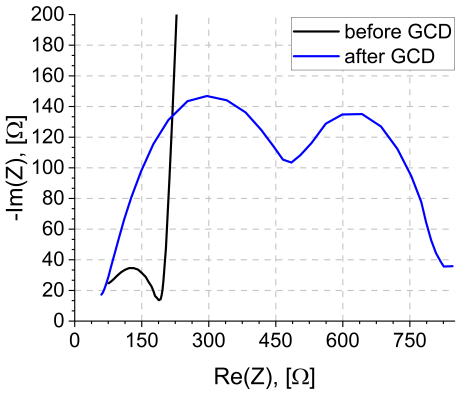

(b) MK100 (23.97 mg; 3.17 mg/cm^2), EIS.

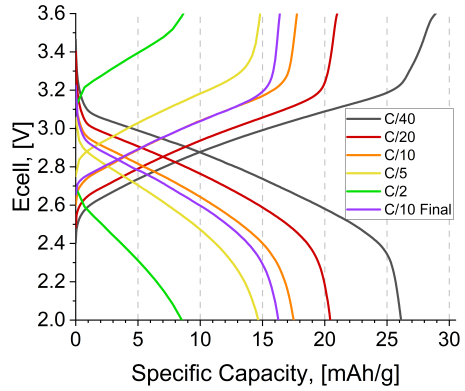

(c) MK52 (23.93 mg; 3.56 mg/cm^2), GCD.

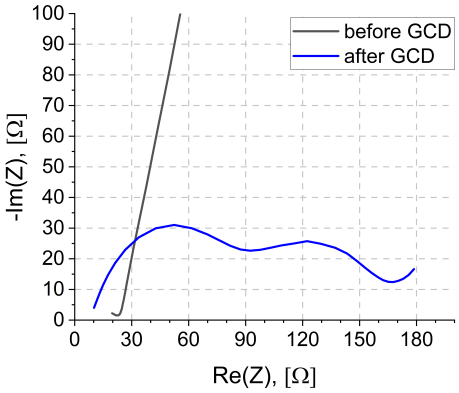

(d) MK52 (23.93 mg; 3.56 mg/cm^2), EIS.

Figure 4.11. Comparison of GCD and EIS data for two full cells with comparable LFP coating masses and the same EPD parameters (80 V/10 min) as per Table 4.8. MK52 contains a balanced negative electrode and liquid electrolyte without SBE, whereas MK100 contains an unbalanced negative electrode and cured SBE.

In Figure 4.12 the voltage profiles and EIS curves for micro- and nano-based LFP full cells with comparable LFP coating masses are displayed. As shown in Figure 4.12b the nano-based SB cell, MK27, despite its lower deposit mass, exhibits higher interface resistance after GCD cycling compared to micro-LFP-based MK35 (Figure 4.12d). Moreover, the comparison of voltage profiles indicates more robust performance for the micro-based full cell (Figure 4.12c), with slightly higher specific capacity values and better operation at higher current rates. Yet, MK35's rate of capacity drop is similar to that of the nano-LFP cell (Figure 4.12a). As for recovery behavior after high discharge rates, both full cells regained their initial capacities at a C/10 rate. These results only highlight the necessity for further research of micro- and nano-based LFP cathode materials to obtain statistical significance for proper conclusions.

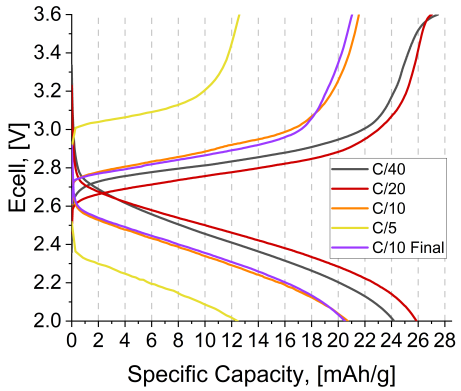

(a) MK27 (12.09 mg; 1.55 mg/cm^2), GCD.

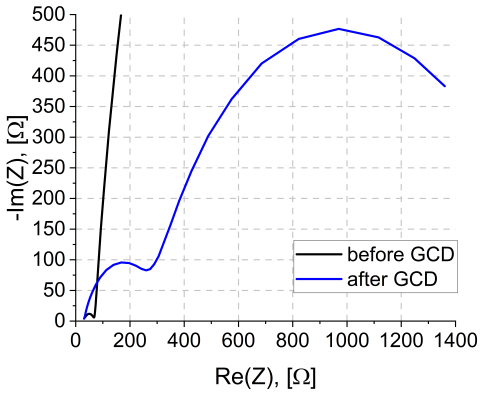

(b) MK27 (12.09 mg; 1.55 mg/cm^2), EIS.

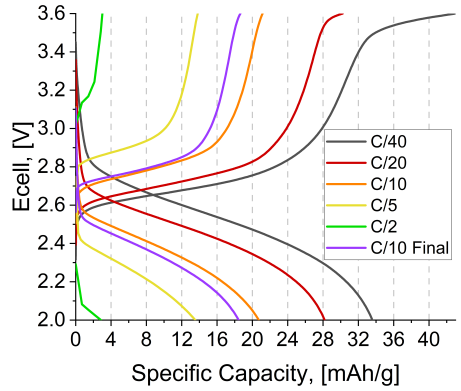

(c) MK35 (13.10 mg; 1.72 mg/cm^2), GCD

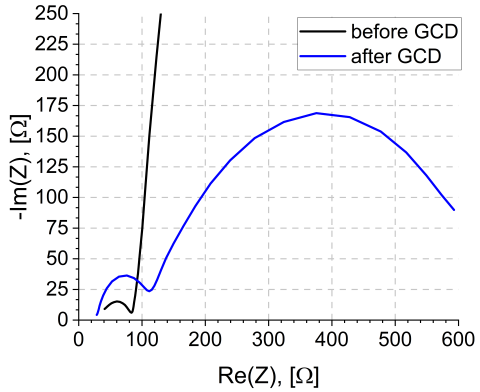

(d) MK35 (13.10 mg; 1.72 mg/cm^2), EIS.

Figure 4.12. Comparison of GCD and EIS data for micro- (MK35) and nano-based (MK27) full cells deposited at 80 V/5 min as per Table 4.8. Both full cells contain unbalanced negative electrodes.

The maximum discharge-specific capacities of each prepared full cell are gathered in Table 4.9. By comparing the deposit mass gains at positive electrodes, we observe an interesting tendency: regardless of the balancing implementation, separator type used, and EPD details, the maximum specific capacity is reached for samples with loadings less than 2 mg/cm^2. Conversely, the capacity of full structural battery cells decreases with higher deposition masses, regardless of whether micro- or nano-LFP is used (MK35 and MK27, respectively). MK52 full cell indicates that the capacity drop is attributed to the presence of SBE (MK52 and MK107 comparison), which, due to its trade-off nature, impacts ionic conductivity more than the separator's thickness. Overall, higher loading does not notably facilitate capacitance growth, as the same result is achieved with nano-LFP deposit (MK52 and MK27 comparison). This leads to the conclusion that for SB full cells, high-loaded nano-LFP-based coatings (more than 3 mg/cm^2) at this stage of SB development do not facilitate capacitance ability.

Table 4.9. Maximum full cells' approximate specific capacity during discharge at the slowest current rate (C/40) along with corresponding deposit masses of positive electrodes.

Sample # HS40	Specific capacity mAh/g	LFP mass, mg	LFP mass, mg/cm^2	Additional notes
MK107	17	20.83	3.18	balanced
MK100	18	23.97	3.17	unbalanced
MK52	26	23.93	3.56	no SBE, balanced
MK35	34	13.10	1.72	unbalanced
MK27	26	12.09	1.55	unbalanced

4.2.3 Shear Resistance

In this subsection, we present the results of shear resistance measurements for selected samples presented in the Table 4.10.

Table 4.10. Shear resistance measurements of selected EPD samples.

Sample #HS40	LFP, mg	EPD parameters	EPD recipe	resistance, Ω
MK131	38.93	80 V/10 min,	2024,	2.87
MK132	16.21	direct	overnight	4.73
MK126	15.20	80 V/5 min,	2024,	4.59
MK129	13.95	direct	overnight	3.67
MK111	19.84	80 V/10 min,	2024*,	3.09
MK110	17.70	direct	overnight	2.15
MK93	39.91	70 V/20 min,	2024,	3.7
MK99	18.08	direct	overnight	6.13
Pristine CFs	-	-	-	3.9

The EPD process parameters such as voltage, time, and direct current were varied to understand their impact on the deposition quality and resultant resistance of the coated electrodes. For instance, sample MK131, which underwent EPD at 80 V for 10 minutes using a direct current and recipe 2024 overnight, demonstrated a resistance of 2.87 Ω. In comparison, sample MK132, processed under identical conditions but with a lower LFP mass of 16.21 mg, showed a higher resistance of 4.73 Ω.

Interestingly, the samples MK93 and MK99, subjected to a lower voltage of 70 V for an extended duration of 20 minutes, exhibited resistivities of 3.7 Ω and 6.13 Ω, respectively. These observations suggest that both the applied voltage and deposition time significantly influence the resistance, with longer deposition times potentially leading to higher resistance values by potentially increasing the thickness of the LFP layer or leading to inhomogeneous deposition.

The pristine CFs exhibited a resistance of 3.9 Ω, serving as a baseline to evaluate the impact of the EPD process on the resistance of the CF electrodes. Most of the coated samples show resistance within a comparable range, confirming that using carbon additives during EPD process generally enhances the conductivity of the CF electrodes when optimal parameters are employed.

In general, the results confirm the fact that EPD parameters significantly impact the shear resistance of the CF electrodes. Higher voltages and longer deposition times generally improve the conductivity of the coatings. However, there is an optimal range for these parameters, outside of which the resistance may increase due to potential inhomogeneous deposition or excessive thickness.

5

Summary and Outlook

This thesis aimed to advance the development of structural batteries by utilising nanosized LFP functionalised high-modulus carbon fibres HS40 as positive electrodes. The core objective was to enhance the multifunctional capabilities of these batteries, integrating mechanical load-bearing properties with efficient energy storage to address the growing demands in applications such as electric vehicles.

The study began by exploring the laminated SB architecture, which includes CF-based electrodes, separators, and structural battery electrolyte. This architecture demonstrated significant potential to provide both mechanical integrity and energy storage. The SBE, incorporating a liquid electrolyte, effectively facilitated ionic transport while bearing mechanical loads, proving its dual functionality.

A critical part of the research involved optimising the EPD process for coating CFs with a blend of nano-LFP, carbon black, and reduced graphene oxide with PDDA as a cationic polyelectrolyte in an ethanol suspension. Parameters such as voltage (70-80 V) and deposition time (10-20 minutes) were essential in achieving uniform and effective coatings.

Electrochemical performance tests of the fabricated electrodes revealed promising specific capacities and stable cycling behaviour, particularly in samples with approximately 20-35 mg of active material. The half-cell results indicated that positive electrodes with nanosized LFP and high-modulus CFs have promising potential for structural batteries. The incorporation of CB and rGO enhanced the electronic conductivity and structural stability of the electrodes, leading to improved overall battery efficiency. However, the all-fibre FCs highlighted the necessity for deeper research, as their performance still showed room for improvement. Factors such as better separator materials could significantly enhance the electrochemical performance of these cells.

Looking forward, several key areas need further exploration to advance this technology. Optimising the EPD process parameters, including voltage, deposition time, and the concentration of CB and rGO, could lead to even better performance and uniformity of the coatings. Additionally, investigating different solvents and dispersing agents might improve the stability and efficiency of the EPD process.

Extended cycling tests and real-world simulations are necessary to evaluate the long-term durability and reliability of these batteries under various conditions. Understanding the degradation mechanisms will be crucial for improving the lifespan of structural batteries.

Future research should also focus on integrating these batteries into practical applications, such as electric vehicles and aerospace structures, to evaluate their practical benefits and challenges. Collaboration with industry partners could facili-

tate the development of scalable manufacturing processes.

Lastly, environmental and economic considerations must be addressed. Life cycle assessments and cost analyses will be important to ensure that the production and use of these batteries are environmentally sustainable and economically viable.

In conclusion, we believe that the advancements in structural battery technology presented in this thesis provide a solid foundation for future innovations. By continuing to explore and optimise these multifunctional materials, significant strides can be made towards more efficient and sustainable energy storage solutions.

Bibliography

1. Heilbron, J. L. *Electricity in the 17th and 18th Centuries: A study of early modern physics* (University of California Press, 2023).
2. Franklin, B. *Experiments and observations on electricity, made at Philadelphia in America* (Printed and sold by E. Cave, at St. John's Gate, 1751).
3. Tucker, T. *Bolt Of Fate: Benjamin Franklin And His Fabulous Kite* (PublicAffairs, 2003).
4. Piccolino, M. Luigi Galvani's path to animal electricity. *Comptes Rendus. Biologies* **329,** 303–318 (2006).
5. Pancaldi, G. *Volta: Science and culture in the age of enlightenment* (Princeton University Press, 2005).
6. Linden, D. & Reddy, T. B. *Linden's Handbook of Batteries* (McGraw-Hill, 2001).
7. Desmond, K. *Innovators in battery technology: Profiles of 93 influential electrochemists* (McFarland and Company, Inc., 2016).
8. Schlesinger, H. *The battery: How portable power sparked a technological revolution* (Harper, 2011).
9. Goodenough, J. B. & Park, K. The Li-ion rechargeable battery: A perspective. *Journal of the American Chemical Society* **135,** 1167–1176 (2013).
10. Ritchie, H. Sector by sector: where do global greenhouse gas emissions come from? *Our World in Data.* https://ourworldindata.org/ghg-emissions-by-sector (2020).
11. Jones, K. B., Jervey, B., Roche, M. & Barnowski, S. *The Electric Battery: Charging forward to a low-carbon future* (Praeger, an imprint of ABC-CLIO, LLC, 2017).
12. Zackrisson, M. *et al.* Prospective life cycle assessment of a structural battery. *Sustainability* **11,** 5679 (2019).
13. Wong, E. L. *et al.* Design and Processing of Structural Composite Batteries. *Proceedings of Society for the Advancement of Materiel and Process Engineering SAMPE 2007 Symposium and Exhibition* (2007).
14. Siraj, M. S. *et al.* Advancing Structural Battery Composites: Robust manufacturing for enhanced and consistent multifunctional performance. *Advanced Energy and Sustainability Research* **4** (2023).
15. Pasquill, B. *Anode vs cathode: Battery definitions* `https://www.ossila.com/pages/anode-vs-cathode-batteries#:~:text=During%20charging%2C%20the%20cathode%20supplies,the%20cathode%20to%20the%20anode`.
16. Asp, L. E. & Greenhalgh, E. S. in *Multifunctionality of Polymer Composites Challenges and New Solutions* 1st ed., 619–661 (William Andrew, 2015).

17. West, D. M. & Karsten, J. *Investment in lithium-ion batteries may crowd out future innovation* 2022. https://www.brookings.edu/articles/investment-in-lithium-ion-batteries-may-crowd-out-future-innovation/.
18. Hagberg, J. *et al.* Lithium iron phosphate coated carbon fiber electrodes for structural lithium ion batteries. *Composites Science and Technology* **162,** 235–243 (2018).
19. Asp, L. E. & Greenhalgh, E. S. Structural Power Composites. *Composites Science and Technology* **101,** 41–61 (2014).
20. Jacques, E. *Lithium-intercalated carbon fibres towards the realisation of multifunctional composite energy storage materials* PhD thesis (KTH School of Engineering Sciences, 2014).
21. Greenhalgh, E. Structural power composites for hybrid vehicles (storage). *ECCM 2012 - Composites at Venice, Proceedings of the 15th European Conference on Composite Materials* (2012).
22. Asp, L. E. *et al.* A structural battery and its multifunctional performance. *Advanced Energy and Sustainability Research* **2** (2021).
23. Sanchez, J. S. *et al.* Electrophoretic coating of LiFePO4/graphene oxide on carbon fibers as cathode electrodes for structural lithium ion batteries. *Composites Science and Technology* **208,** 108768 (2021).
24. Carlstedt, D., Runesson, K., Larsson, F., Xu, J. & Asp, L. E. Electro-chemo-mechanically coupled computational modelling of structural batteries. *Multifunctional Materials* **3,** 045002 (2020).
25. Asp, L. E., Johansson, M., Lindbergh, G., Xu, J. & Zenkert, D. Structural Battery Composites: A Review. *Functional Composites and Structures* **1,** 042001 (2019).
26. Drzal, L. T., Rich, M. J., Koenig, M. F. & Lloyd, P. F. Adhesion of graphite fibers to epoxy matrices: II. the effect of Fiber Finish. *The Journal of Adhesion* **16,** 133–152 (1983).
27. O'Brien, T. K. *Composite materials: Fatigue and fracture* (ASTM, 1991).
28. https://www.epsilon-composite.com/en/carbon-fiber-grades.
29. Jang, J. *et al.* Turbostratic nanoporous carbon sheet membrane for ultrafast and selective nanofiltration in viscous green solvents. *Journal of Materials Chemistry A* **8,** 8292–8299 (2020).
30. Fredi, G. *et al.* Graphitic microstructure and performance of carbon fibre Li-ion structural battery electrodes. *Multifunctional Materials* **1,** 015003 (2018).
31. Northolt, M., Veldhuizen, L. & Jansen, H. Tensile deformation of carbon fibers and the relationship with the modulus for shear between the basal planes. *Carbon* **29,** 1267–1279 (1991).
32. Fitzer, E. & Manocha, L. M. *Carbon reinforcements and carbon/carbon composites* (Springer, 1998).
33. Hajizadeh, A. *et al.* Electrophoretic deposition as a fabrication method for Li-ion battery electrodes and separators - a review. *Journal of Power Sources* **535,** 231448 (2022).
34. Diba, M., Fam, D. W., Boccaccini, A. R. & Shaffer, M. S. Electrophoretic deposition of graphene-related materials: A review of the fundamentals. *Progress in Materials Science* **82,** 83–117 (2016).

35. Chakrabarti, B. K. *et al.* Modern practices in electrophoretic deposition to manufacture energy storage electrodes. *International Journal of Energy Research* **46,** 13205–13250 (2022).
36. Moosburger-Will, J. *et al.* Interaction between carbon fibers and polymer sizing: Influence of fiber surface chemistry and sizing reactivity. *Applied Surface Science* **439,** 305–312 (2018).
37. Kjell, M. H., Jacques, E., Zenkert, D., Behm, M. & Lindbergh, G. PAN-Based carbon fiber negative electrodes for structural lithium-ion batteries. *Journal of The Electrochemical Society* **158** (2011).
38. Snyder, J. F., Wong, E. L. & Hubbard, C. W. Evaluation of commercially available carbon fibers, fabrics, and papers for potential use in multifunctional energy storage applications. *Journal of The Electrochemical Society* **156** (2009).
39. Xia, Z. *et al.* Green synthesis of positive electrodes for high performance structural batteries - A study on graphene additives. *Composites Science and Technology* **251,** 110568 (2024).
40. Jacques, E. *et al.* Impact of electrochemical cycling on the tensile properties of carbon fibres for structural lithium-ion composite batteries. *Composites Science and Technology* **72,** 792–798 (2012).

DEPARTMENT OF INDUSTRIAL AND MATERIALS SCIENCE
CHALMERS UNIVERSITY OF TECHNOLOGY
Gothenburg, Sweden
www.chalmers.se

CHALMERS
UNIVERSITY OF TECHNOLOGY